

Active tectonic field for CO₂ Storage management: Hontomín onshore study-case (SPAIN)

Raúl Pérez-López¹, José F. Mediato¹, Miguel A. Rodríguez-Pascua¹, Jorge L. Giner-Robles², Adrià Ramos¹, Silvia Martín-Velázquez³, Roberto Martínez-Orío¹, Paula Fernández-Canteli¹

1. IGME – Instituto Geológico y Minero de España – Geological Survey of Spain. C/Ríos Rosas 23, Madrid 28003 – SPAIN. Email: r.perez@igme.es, jf.mediato@igme.es, ma.rodriguez@igme.es, a.ramos@igme.es, ro.martinez@igme.es, paula.canteli@igme.es

2. Departamento de Geología y Geoquímica. Facultad de Ciencias. Universidad Autónoma de Madrid. Campus Cantoblanco, Madrid. SPAIN. Email: jorge.giner@uam.es

3. Universidad Rey Juan Carlos. Email: silvia.martin@urjc.es

Abstract

One of the concerns of underground CO₂ onshore storage is the triggering of Induced Seismicity and fault reactivation by pore pressure increasing. Hence, a comprehensive analysis of the tectonic parameters involved in the storage rock formation is mandatory for safety management operations. Unquestionably, active faults and seal faults depicting the storage bulk are relevant parameters to be considered. However, there is a lack of analysis of the active tectonic strain field affecting these faults during the CO₂ storage monitoring. The advantage of reconstructing the tectonic field is the possibility to determine the strain trajectories and describing the fault patterns affecting the reservoir rock. In this work, we adapt a methodology of systematic geostructural analysis to the underground CO₂ storage, based on the calculation of the strain field and defined by the strain field from kinematics indicators on the fault planes (e_y and e_x for the maximum and minimum horizontal shortening respectively). This methodology is based on a statistical analysis of individual strain tensor solutions obtained from fresh outcrops from Triassic to Miocene. Consequently, we have collected 447 fault data in 32 field stations located within a 20 km radius. The understanding of the fault sets role for underground fluid circulation can also be established, helping for further analysis of CO₂ leakage and seepage. We have applied this methodology to Hontomín onshore CO₂

32 storage facilities (Central Spain). The geology of the area and the number of high-
33 quality outcrops made this site as a good candidate for studying the strain field from
34 kinematics fault analysis. The results indicate a strike-slip tectonic regime with the
35 maximum horizontal shortening with N160°E and N50°E trend for the local regime,
36 which activates NE-SW strike-slip faults. A regional extensional tectonic field was also
37 recognized with N-S trend, which activates N-S extensional faults, and NNE-SSW and
38 NNW-SSE strike-slip faults, measured in the Cretaceous limestone on top of the
39 Hontomín facilities. Monitoring these faults within the reservoir is suggested in addition
40 to the possibility of obtaining focal mechanism solutions for microearthquakes ($M < 3$).

41

42 Keywords: onshore CO₂ storage, tectonic field, paleostrain analysis, active fault,
43 Hontomín onshore pilot-plant.

44

45 1. INTRODUCTION

46 Industrial made-man activities generate CO₂ that could change the chemical balance of
47 the atmosphere and their relationship with the geosphere. The Geological Carbon
48 Storage (GSC) appears as a good choice to reduce the CO₂ gas emission to the
49 atmosphere (Christensen, 2004), allowing the industry increasing activity with a low
50 pollution impact. There is a lot of literature about what must have a site to be a potential
51 underground storage suitable to GSC (e.g. Chu, 2009; Orr, 2009; Goldberg et al., 2010
52 among others). The reservoir sealing, the caprock, permeability and porosity, plus
53 injection pressure and volume injected, are the main considerations to choose one
54 geological subsurface formation as the CO₂ host-rock. In this frame, the tectonic active
55 field is considered in two principal ways: (1) to prevent the fault activation and
56 earthquakes triggering, with the consequence of leakage and seepage, and (2) the long-

57 term reservoir behavior, understanding as long-term from centennial to millennial time-
58 span. Therefore, what is the long-term behavior of GSC? What do we need to monitor
59 for a safe GSC management? [Winthaegen et al. \(2005\)](#) suggest three subjects for
60 monitoring: (a) the atmosphere air quality near the injection facilities, due to the CO₂
61 toxicity (values greater than 4%, see [Rice, 2003](#) and [Permentier et al., 2017](#)), (b) the
62 overburden monitoring faults and wells and (c) the sealing of the reservoir. The study of
63 natural analogues for GSC is a good strategy to estimate the long-term behavior of the
64 reservoir, considering parameters as the injected CO₂ pressure and volume, plus the
65 brine mixing with CO₂ ([Pearce, 2006](#)). Hence, the prediction of site performance over
66 long timescales also requires an understanding of CO₂ behavior within the reservoir, the
67 mechanisms of migration out of the reservoir, and the potential impacts of a leak on the
68 near surface environment. The assessments of such risks will rely on a combination of
69 predictive models of CO₂ behavior, including the fluid migration and the long-term
70 CO₂-porewater-mineralogical interactions ([Pearce, 2006](#)). Once again, the tectonic
71 active field interacts directly on this assessment. Moreover, the fault reactivation due to
72 the pore pressure increasing during the injection and storage has also to be considered
73 ([Röhmman et al., 2013](#)). Despite the uplift measure by [Röhmman et al. \(2013\)](#) are
74 submillimeter (c.a. 0.021 mm) at the end of the injection processes, given the ongoing
75 occurrence of microearthquakes, long-term monitoring is required. The geomechanical
76 and geological models predict the reservoir behavior and the caprock sealing properties.
77 The role of the faults inside these models is crucial for the tectonic long-term behavior
78 and the reactivation of faults that could trigger earthquakes.

79 Concerning the Induced Seismicity, [Wilson et al. \(2017\)](#) published the Hi-Quake
80 database, with a classification of all man-made earthquakes according to the literature,
81 in an online repository (<https://inducedearthquakes.org/>, last access on May, 2019). This

82 database includes 834 projects with proved Induced Seismicity, where two different
83 cases with earthquakes as large as M 1.7, detected in swarms about 9,500
84 microearthquakes, are related to GSC operations. Additionally, [Foulger et al. \(2018\)](#)
85 pointed out that GSC can trigger earthquakes with magnitudes lesser than M 2, namely
86 the cases described in their work are as great as M 1.8, with the epicenter location 2 km
87 around the facilities. [McNamara \(2016\)](#) described a comprehensive method and
88 protocol for monitoring GSC reservoir for the assessment and management of Induced
89 Seismicity. The knowledge of active fault patterns and the stress/strain field could help
90 on designing monitoring network and identifying those faults capable of triggering
91 micro-earthquakes ($M < 2$) and/or breaking the sealing for leakage (patterns of open
92 faults for low-permeability CO₂ migration).

93 In this work, we propose that the description, the analysis and establishment of the
94 tectonic strain field have to be mandatory for long-term GSC monitoring and
95 management, implementing the fault behavior in the geomechanical models. This
96 analysis does not increase the cost for long-term monitoring, given that they are low-
97 cost and the results are acquired in a few months. Therefore, we propose a methodology
98 based on the reconstruction of the strain field from the classical studies in geodynamics
99 ([Angelier, 1979 and 1984](#); [Reches, 1983](#); [Reches, 1987](#)). As a novelty, we introduce the
100 strain fields (SF) analysis between 20 away from the subsurface reservoir deep
101 geometry, under the area of influence of induced seismicity for fluid injection. The
102 knowledge of the strain field at local scale allows classifying the type of faulting and
103 their role for leakage processes, whilst the regional scale explores the tectonic active
104 faults that could affect the reservoir. The methodology is rather simple, taking measures
105 of slickensides and striations on fault planes to establish the orientation of the maximum
106 horizontal shortening (e_y), and the minimum horizontal shortening (e_x) for the strain

107 tensor. The principal advantage of the SF analysis is the directly classification of all the
108 faults involved into the geomechanical model and the prediction of the failure
109 parameters. Besides, a Mohr-Coulomb failure analysis was performed to the fault
110 pattern recognized in the Cretaceous outcrop located on top of the pilot plant.

111 The tectonic characterization of the GSC of Hontomín was implemented in the
112 geological model described by [Le Gallo and de Dios \(2018\)](#). Beyond the use of Induced
113 Seismicity and potentially active faults, the scope of this method is to propose an initial
114 analysis to manage underground storage operations. We present how the Structural
115 Analysis of fault/slip data can improve the knowledge of the tectonic large-scale fault
116 network for the potential seismic reactivation during fluid injection and time-depend
117 scale for fluid stays.

118

119 2. HONTOMÍN ONSHORE STUDY CASE

120 *2.1 Geological description of the reservoir*

121 The CO₂ storage site of Hontomín is enclosed in the southern section of the Mesozoic
122 Basque–Cantabrian Basin, known as Burgalesa Platform ([Serrano and Martínez del](#)
123 [Olmo, 1990](#); [Tavani, 2012](#)), within the sedimentary Bureba Basin (**Fig. 1**). This
124 geological domain is located in the northern junction of the Cenozoic Duero and Ebro
125 basins, forming an ESE-dipping monocline bounded by the Cantabrian Mountains
126 Thrust to the north, the Ubierna Fault System (UFS) to the south and the Asturian
127 Massif to the west (**Fig. 1**).

128 The Meso-Cenozoic tectonic evolution of the Burgalesa Platform starts with a first rift
129 period during Permian and Triassic times ([Dallmeyer and Martínez-García, 1990](#);
130 [Calvet et al., 2004](#)), followed by a relative tectonic quiescence during Early and Middle
131 Jurassic times (e.g. [Aurell et al., 2002](#)). The main rifting phase took place during the

132 Late Jurassic and Early Cretaceous times, due to the opening of the North Atlantic and
133 the Bay of Biscay-Pyrenean rift system (García-Mondéjar et al., 1986; Le Pichon and
134 Sibuet, 1971; Lepvrier and Martínez-García, 1990; García-Mondéjar et al., 1996; Roca
135 et al., 2011; Tugend et al., 2014). The convergence between Iberia and Eurasia from
136 Late Cretaceous to Miocene times triggered the inversion of previous Mesozoic
137 extensional faults and the development of an E-W orogenic belt (Cantabrian domain to
138 the west and Pyrenean domain to the east) formed along the northern Iberian plate
139 margin (Muñoz, 1992; Gómez et al., 2002; Vergés et al., 2002).

140 The Hontomín facilities are located within the Basque-Cantabrian Basin (**Fig. 1b**). The
141 geological reservoir structure is bordered by the UFS to the south and west, by the Poza
142 de la Sal diapir and the Zamanzas Popup structure (Carola, 2014) to the north and by the
143 Ebro Basin to the east (**Fig. 1**). The structure is defined as a forced fold related dome
144 structure (Tavani et al., 2013; **Fig. 2**), formed by an extensional fault system with
145 migration of evaporites towards the hanging wall during the Mesozoic (Soto et al.,
146 2011). During the tectonic compressional phase, associated with the Alpine Orogeny
147 affecting the Pyrenees, the right-lateral transpressive inversion of the basement faults
148 was activated, along with the reactivation of transverse extensional faults (**Fig. 2**;
149 Tavani et al., 2013; Alcalde et al., 2014).

150 The target reservoir and seal formations consist of Lower Jurassic marine carbonates,
151 arranged in an asymmetric dome-like structure (**Fig. 2**) with an overall extent of 15 km²
152 and located at 1,485 m of depth (Alcalde et al., 2013, 2014; Ogaya et al., 2013). The
153 target CO₂ injection point is a saline aquifer formed by a dolostone unit, known as
154 “Carniolas”, and an oolitic limestone of the Sopeña Formation, both corresponding to
155 Lias in time (Early Jurassic). The estimated porosity of the Carniolas reaches over 12%
156 (Ogaya et al., 2013; Le Gallo and de Dios, 2018) and it is slightly lower at the

157 Carbonate Lias level (8.5% in average). The reservoir levels contain saline water with
158 more than 20 g/l of NaCl and very low oil content. The high porosity of the lower part
159 of the reservoir (i.e., the Carniolas level) is the result of secondary dolomitization and
160 different fracturing events (Alcalde et al., 2014). The minimum thickness of the
161 reservoir units is 100 m. The potential upper seal unit comprises Lias marlstones and
162 black shales from a hemipelagic ramp (Fig. 2); Pliensbachian and Toarcian) of the
163 “Puerto del Pozazal” and Sopeña Formations.

164

165 *2.2 Regional tectonic field*

166 The tectonic context has been described from two different approaches: (1) the tectonic
167 style of the fractures bordering the Hontomín reservoir (De Vicente et al., 2011; Tavani
168 et al., 2011) and (2) the tectonic regional field described from earthquakes with
169 mechanism solutions and GPS data (Herraiz et al., 2000; Stich et al., 2006; De Vicente
170 et al., 2008).

171 (1) The tectonic style of the Bureba Basin was described by De Vicente et al. (2011),
172 which classified the Basque-Cantabrian Cenozoic Basin (Fig. 1a) as transpressional
173 with contractional horsetail splay basin. The NW-SE oriented Ventaniella fault (Fig.
174 1a), includes the UFS in the southeastward area, being active between the Permian and
175 Triassic period, and strike-slip during the Cenozoic contraction. In this tectonic
176 configuration, the Ubierna Fault acts as a right-lateral strike-slip fault. These authors
177 pointed out the sharp contacts between the thrusts and the strike-slip faults in this basin.
178 Furthermore, Tavani et al. (2011) also described complex Cenozoic tectonic context
179 where right-lateral tectonic style reactivated WNW-ESE trending faults. Both the
180 Ventaniella and the Ubierna faults acted as transpressive structures forming 120 km
181 long and 15 km wide of the UFS, and featured by 0.44 mm/yr of averaged tectonic

182 strike-slip deformation between the Oligocene and the present day. The aforementioned
183 authors described different surface segments of the UFS of right-lateral strike-slip
184 ranging between 12 and 14 km length. The structural data collected by [Tavani et al.](#)
185 [\(2011\)](#) pointed out the 60% of data correspond to right lateral strike-slip with WNW-
186 ESE trend, together with conjugate reverse faulting with NE-SW, NW-SE and E-W
187 trend, and left-lateral strike-slip faults N-S oriented. They concluded that this scheme
188 could be related to a transpressional right-lateral tectonic system with a maximum
189 horizontal compression, S_{Hmax} , striking N120°E. Concerning the geological evidence of
190 recent sediments affected by tectonic movements of the UFS, [Tavani et al. \(2011\)](#)
191 suggest Middle Miocene in time for this tectonic activity. However, geomorphic
192 markers (river and valley geomorphology) could indicate tectonic activity at present-
193 times. All of these data correspond to regional or small-scale data collected to explain
194 the Basque-Cantabrian Cenozoic transpressive basin. The advantage of the
195 methodology proposed here to establish the tectonic local regime affecting the reservoir,
196 is the searching for local-scale tectonics (20 km sized), and the estimation of the depth
197 for the non-deformation surface for strata folding in transpressional tectonics ([Lisle et](#)
198 [al., 2009](#)).

199 (2) Regarding the stress field from earthquake focal mechanism solutions, [Herraiz et al.](#)
200 [\(2000\)](#) pointed out the regional trajectories of S_{Hmax} with NNE-SSW trend, and with a
201 NE-SW S_{Hmax} trend from slip-fault inversion data. [Stich et al. \(2006\)](#) obtained the stress
202 field from seismic moment tensor inversion and GPS data. These authors pointed out a
203 NW-SE Africa-Eurasia tectonic convergence at tectonic rate of 5 mm/yr approximately.
204 However, no focal mechanism solutions are found within the Hontomín area (20 km)
205 and only long-range spatial correlation could be made with high uncertainty (in time,
206 space and magnitude). The same lack of information appears in the work of [De Vicente](#)

207 [et al. \(2008\)](#), with no focal mechanism solutions in the 50 km surrounding the HPP. In
208 this work, these authors classified the tectonic regime as uniaxial extension to strike-slip
209 with NW-SE S_{Hmax} trend.
210 Regional data about the tectonic field inferred from different works ([Herraiz et al.,](#)
211 [2000](#); [Stich et al., 2006](#); [De Vicente et al., 2008, 2011](#); [Tavani et al., 2011](#); [Tavani,](#)
212 [2012](#)), show differences for the S_{Hmax} . These works explain the tectonic framework for
213 regional scale. Nevertheless, local tectonics could determine the low permeability and
214 the potential induced seismicity within the reservoir. In the next section, we have
215 applied the methodology described at the section 3 of this manuscript, in order to
216 compare the regional results from these works and to establish the tectonic evolution of
217 the Burgalesa Platform.

218

219 *2.3 Strategy of the ENOS European Project*

220 Hontomín pilot-plant (HPP) for CO₂ onshore storage is the only one in Europe
221 recognized as a key-test-facility, and it is managed and conducted by CIUDEN
222 (*Fundación Ciudad de la Energía*). The HPP is located within the province of Burgos
223 (**Fig. 1b**), in the northern central part of Spain.

224 The methodology proposed in this work and its application for long-term onshore GSC
225 managing in the frame of geological risk, is based on the strain tensor calculation, as
226 part of the objectives proposed in the European project “ENabling Onshore CO₂
227 Storage in Europe” (ENOS). The ENOS project is an initiative of CO₂GeoNet, the
228 European Network of Excellence on the geological storage of CO₂ for supporting
229 onshore storage and fronting the associated troubles as GSC perception, the safe storage
230 operation, potential leaking management and health, and environmental safety ([Gastine](#)
231 [et al., 2017](#)). ENOS combines a multidisciplinary European project, which focuses in

232 onshore storage, with the demonstration of best practices through pilot-scale projects in
233 the case of Hontomín facilities. Moreover, this project claims for creating a favorable
234 environment for GSC onshore through public engagement, knowledge sharing, and
235 training (Gastine et al., 2017). In this context, the work-package WP1 is devoted to
236 “ensuring safe storage operations”.

237

238 3. METHODS AND RATIONALE

239 The lithosphere remains in a permanent state of deformation, related to plate tectonics
240 motion. Strain and stress fields are the consequence of this deformation on the upper
241 lithosphere, arranging different fault patterns that determine sedimentary basins and
242 geological formations. Kinematics of these faults describes the stress/strain fields, for
243 example measuring grooves and slickensides on fault planes (see Angelier, 1979,
244 Reches, 1983 among others). The relevance of the tectonic field is that stress and strain
245 determine the earthquake occurrence by the fault activity. In this work, we have
246 performed a brittle analysis of the fault kinematics, by measuring slickenfiber on fault
247 planes (dip/ dip direction and rake), in several outcrops in the surroundings of the
248 onshore reservoir. To carry out the methodology proposed in this work, the study area
249 was divided in a circle with four equal areas, and we searched outcrops of fresh rock to
250 perform the fault kinematic analysis. This allows establishing a realistic tectonic very-
251 near field to be considered during the storage seismic monitoring and long-term
252 management. Finally, we have studied the fault plane reactivation by using the Mohr-
253 Coulomb failure criterion (Pan et al., 2016), from the fault pattern obtained in the
254 Cretaceous limestone outcrop located on top of the HPP facilities.

255

256 3.1 *Paleostrain Analysis*

257 We have applied the strain inversion technique to reconstruct the tectonic field
258 (paleostrain evolution), affecting the Hontomín site between the Triassic, Jurassic,
259 Cretaceous and Neogene ages (late Miocene to present times). For a further
260 methodology explanation, see [Etchecopar et al. \(1981\)](#), [Reches \(1983\)](#) and [Angelier](#)
261 [\(1990\)](#). The main assumption for the inversion technique of fault population is the self-
262 similarity to the scale invariance for the stress/strain tensors. This means that we can
263 calculate the whole stress/strain fields by using the slip data on fault planes and for
264 homogeneous tectonic frameworks. The strain tensor is an ellipsoid defined by the
265 orientation of the three principal axes and the shape of the ellipsoid (k). This method
266 assumes that the slip-vectors, obtained from the pitch of the striation on different fault
267 planes, define a common strain tensor or a set in a homogeneous tectonic arrangement.
268 We assume that the strain field is homogeneous in space and time, the number of faults
269 activated is greater than five and the slip vector is parallel to the maximum shear stress
270 (τ).

271 The inversion technique is based on the Bott equations ([Bott, 1959](#)). These equations
272 show the relationship between the orientation and the shape of the stress ellipsoid:

273

$$274 \quad \tan(\theta) = [n / (1 * m)] * [m^2 - (1 - n^2) * R'] \quad [\text{eq.1}]$$

$$275 \quad R' = (\sigma_z - \sigma_x) / (\sigma_y - \sigma_x) \quad [\text{eq.2}]$$

276

277 Where l , m and n are the direction cosines of the normal to the fault plane, θ is the pitch
278 of the striation and R' is the shape of the stress ellipsoid obtained in an orthonormal
279 coordinate system, x , y , z . In this system, σ_y is the maximum horizontal stress, σ_x is the
280 minimum horizontal stress axis and σ_z is the vertical stress axis.

281

282 3.2 The Right-Dihedral Model for Paleostrain Analysis

283 The Right-Dihedral (RD) is a semi-quantitative method based on the overlapping of
284 compressional and extensional zones by using a stereographic plot. The final plot is an
285 interferogram figure, which usually defines the strain-regime. This method is strongly
286 robust for conjugate fault sets and with different dip values for a same tensor. The RD
287 was originally defined by Pegoraro (1972) and Angelier and Mechler (1977), as a
288 geometric method, adjusting the measured fault-slip data (slickensides) in agreement
289 with theoretical models for extension and compressive fault-slip. Therefore, we can
290 constraint the regions of maximum compression and extension related to the strain
291 regime.

292

293 3.3 The Slip Model for the Paleostrain Analysis

294 The Slip Model (SM) is based on the Navier-Coulomb fracturing criteria (Reches,
295 1983), taking the Anderson model solution for this study (Anderson, 1951; Simpson,
296 1997). The Anderson model represents the geometry of the fault plane as monoclinic,
297 relating the quantitative parameters of the shape parameter (K') with the internal
298 frictional angle for rock mechanics (ϕ) (De Vicente 1988; Capote et al., 1991).
299 Moreover, this model is valid for neofomed faults, and some considerations have to be
300 accounted for previous faults and weakness planes present in the rock. These
301 considerations are related to the dip of normal and compressional faults, such as for
302 compressional faulting dip values lower than 45° , reactivated as extensional faults. This
303 model shows the relationships between the K' , ϕ and the direction cosines for the
304 striation on the fault plane (De Vicente, 1988; Capote et al., 1991):

305

$$306 \quad K' = e_y / e_z \quad \text{[eq.3]}$$

307

308 Where e_z is the vertical strain axis, e_y is the maximum horizontal shortening and e_x is
309 the minimum horizontal shortening. This model assumes that there is no change of
310 volume during the deformation and $e_y = e_x + e_z$.

311 For isotropic solids, principal strain axes coincide with the principal stress axes. This
312 means that in this work, the orientation of the principal stress axis, S_{Hmax} is parallel to
313 the orientation of the principal strain axes, e_y , and hence, the minimum stress axis, S_{hmin} ,
314 is parallel to the minimum strain axis, e_x . This assumption allows us to estimate the
315 stress trajectories (S_{Hmax} and S_{hmin}) from the e_y SM results.

316 Resolving the equations of Anderson for different values (Anderson, 1951), we can
317 classify the tectonic regime that activates one fault from the measurement of the fault
318 dip, sense of dip (0° - 360°) and pitch of the slickenside, assuming that one of the
319 principal axes (e_x , e_y or e_z) is vertical (Angelier, 1984). We can classify the tectonic
320 regime and represent the strain tensor by using the e_y and e_x orientation.

321

322 *3.4 The K' strain diagram*

323 Another analysis can be achieved by using the K' -strain diagram developed by Kaverina
324 et al. (1996) and codified in python-code by Álvarez-Gómez (2014). These authors have
325 developed a triangular representation based on the fault-slip, where tectonic patterns can
326 be discriminated between strike-slip and dip-slip types. This diagram is divided in 7
327 different zones according to the type of fault: (1) pure normal, (2) pure reverse and (3)
328 pure strike-slip; combined with the possibility of oblique faults: (4) reverse strike-slip
329 and (5) strike-slip with reverse component; and lateral faults: (6) normal strike-slip and
330 (7) strike-slip faults with normal component (**Fig. 3**). Strike-slip faults are defined by
331 small values for pitch ($p < 25^\circ$), and dips close to vertical planes ($\beta > 75^\circ$). High pitch

332 values ($p > 60^\circ$) are related to normal or/reverse fault-slip vectors. Extensional faults
333 show e_y in vertical whereas compressional faults show e_y in horizontal plane.

334 This method was originally performed for earthquake focal mechanism solutions by
335 using the focal parameters, the nodal planes (dip and strike) and rake (Kaverina et al.,
336 1996). The triangular graph is based on the equal-area representation of the T, N or B
337 and P axes in spherical coordinates (T tensile, N or B neutral and P pressure axes), and
338 the orthogonal regression between earthquake magnitudes M_s and m_b for the Harvard
339 earthquake CMT global catalogue in 1996. [Álvarez-Gómez \(2014\)](#) presented a code
340 python-based for computing the Kaverina diagrams, and we have modified the input
341 parameters by including the K' intervals for the strain field from the SM. The
342 relationship between the original diagram of Kaverina (**Fig. 3a**) and the K' -dip diagram
343 (**Fig. 3b**) that we have used in this work is shown in the figure 3. The advantage of this
344 diagram is the fast assignation of the type of fault and the tectonic regime that determine
345 this fault pattern, and the strain axes relationship.

346 Table 1 summarizes the different tectonic regimes of the figure 3b showing the
347 relationship with the strain main axes e_y , e_x and e_z . This diagram exhibits a great
348 advantage to classify the type of fault according to the strain tensor. Therefore, we can
349 assume the type of fault from the fault orientation affecting geological deposits for each
350 strain tensor obtained.

351

352 *3.5 The Circular-Quadrant-Search (CQS) strategy for the paleostain analysis*

353 In this work, we propose a low-cost strategy based on a well-known methodology for
354 determining the stress/strain tensor affecting a GSC reservoir, which will allow the
355 long-term monitoring of the geological and seismic behavior (**Fig. 4**). The objective is
356 to obtain enough structural data and spatially homogeneous of faults (**Figs. 4, 5**) for
357 reconstructing the stress/strain tensor. The key-point is the determination of the

358 orientation of the e_y , e_x and K' to plot in a map and therefore, to establish the tectonic
359 regime. We have chosen quadrants of the circles with the aim to obtain a high-quality
360 spatial distribution of point for the interpretation of the local and very near strain field.
361 Hence, data are homogeneously distributed, instead of being only concentrated in one
362 quadrant of the circle.

363 [Pérez-López et al. \(2018\)](#) carried out a first approach to the application of this
364 methodology at Hontomín, under the objective of the ENOS project (see next section
365 for further details). We propose a circular searching of structural field stations (**Figs. 4,**
366 **5**), located within a 20 km radius. This circle was taken, given that active faults with the
367 capacity of triggering earthquakes of magnitudes close to M 6, exhibits a surface rupture
368 of tens of kilometers, according to the empirical models ([Wells and Coppersmith,](#)
369 [1994](#)). Moreover, [Verdon et al. \(2015\)](#) pointed out that the maximum distance of
370 induced earthquakes for fluid injection is 20 km. Larger distances could not be related
371 to the stress/strain regime within the reservoir, except for the case of large geological
372 structures (folds, master faults, etc.). Microseismicity in GSC reservoir is mainly related
373 to the operations during the injection/depletion stages and long-term storage ([Verdon](#)
374 [2014](#); [Verdon et al., 2015](#); [McNamara, 2016](#)).

375 The presence of master faults (capable to trigger earthquakes of magnitude = or > than 6
376 and 5 km long segment) inside the 20 km radius circle, implicates that the regional
377 tectonic field determines the strain accumulation in kilometric fault-sized. Furthermore,
378 the presence of master faults could increase the occurrence of micro-earthquakes, due to
379 the presence of secondary faults prone to trigger earthquakes by their normal seismic
380 cycle ([Scholz, 2018](#)). Bearing in mind that GSC onshore reservoirs use to be deep saline
381 aquifers (e.g. [Bentham and Kirby, 2005](#)) as the Hontomín case ([Gastine et al., 2017](#), [Le](#)
382 [Gallo and de Dios, 2018](#)), which is confined in folded and fractured deep geological

383 structures, in which local tectonics plays a key role in micro-seismicity and the
384 possibility of CO₂ leakage.

385 The constraints of this strategy are related to the absence of kinematics indicators on
386 fault planes. It could occur due to later overlapping geological processes as neoformed
387 mineralization. Also, a low rigidity eludes the slicken fiber formation, and no
388 kinematic data will be marked on the fault plane.. A poor spatial distribution of the
389 outcrops was also taken into account for constraining the strategy. The age of sediments
390 does not represent the age of the active deformations and hence, the active deformation
391 has to be analyzed by performing alternative methods (i.e. paleoseismology,
392 archaeoseismology).

393

394 4. RESULTS

395 *4.1 Strain Field Analysis*

396 We have collected 447 fault-slip data on fault planes in 32 outcrops, located within a 20
397 km radius circle centered at the HPP (**Fig. 5**). The age of the outcrops ranges between
398 Early Triassic to post-Miocene and are mainly located in Cretaceous limestone and
399 dolostone (**Fig. 5, Table 2**). However, no Jurassic outcrops were located, and only
400 seven stations are located on Neogene sediments, ranging between Early Oligocene to
401 Middle-Late Miocene. The small number of Neogene stations is due to the mechanical
402 properties of the affected sediments, mainly poor-lithified marls and soft-detrital fluvial
403 deposits. Despite that, all the Neogene stations exhibit high-quality data with a number
404 of fault-slip data ranging between 7 and 8, enough for a minimum quality analysis.

405 We have labeled the outcrops with the acronym HTM followed by a number (see **figure**
406 **5** for the geographical location and **Table 2** and **figure 6** for the fault data). The station
407 with the highest number of faults measured is HTM17 with 105 faults on Cretaceous

408 limestone. Conjugate fault systems can be recognized in most of the stations (HTM1, 3,
409 5, 7, 10, 14, 16, 21, 23, 24, 25, 29, 30 and 32, **Fig. 6**), although there are a few stations
410 with only one well defined fault set (6, 22, 32). We have to bear in mind that the
411 recording of conjugate fault systems is more robust for the brittle analysis than
412 recording isolated fault sets, better constraining the solution ([Žaholar and Vrabec,](#)
413 [2008](#)). In total, 29 of 32 stations were used (HTM24, 27, 28 with no quality data), and
414 from these 29 stations, 21 were analyzed with the paleostrain technique. Solutions
415 obtained here are robust to establish the paleostrain field in each outcrop as the
416 orientation of the e_y , S_{Hmax} (**Fig. 7**).

417 The results obtained from the application of the paleostrain method have been expressed
418 in stereogram, right dihedral (RD), slip method (SM) and K' - diagram (**Fig. 7**). The K' -
419 diagram shows the fault classification as normal faults, normal with strike-slip
420 component, pure strike-slip, strike-slip with reverse component and reverse faults (see
421 **Fig. 3**). Main faults are lateral strike-slips and normal faults, followed by reverse faults,
422 strike-slips and oblique strike-slips faults. The results of the strain regime are as
423 follows: 1) 43% of extensional with shear component; 2) 22% of shear; 3) 13% of
424 compressive strain (lower Cretaceous and early-middle Miocene, **Table 2**); 4) 13% of
425 pure shear and 5) 9% of shear with compression strain field, although with the presence
426 of five reverse faults.

427 In contrast, we can observe that there are solutions with a double value for the e_y , S_{Hmax}
428 orientation: HTM1, 2, 10, 11, 13, 15, 19, 26, and 30. The stations HTM3 and 23 (upper
429 Cretaceous), show the best solution for strike-slip strain field as a pure strike-slip
430 regime and e_y with N25°E and N99°E trend, respectively (**Fig. 7**).

431 It is easy to observe the agreement between the e_y results from the SM and the K' - strain
432 diagram, for instance, in the HTM2 the K' -diagram indicates strike-slip faults with

433 reverse component for low dips ($0^\circ < \beta < 40^\circ$), but also indicates strike-slip faults with
434 normal component for larger dips ($40^\circ < \beta < 90^\circ$). However, both results are in
435 agreement with a strain field defined by the orientation for e_y , S_{Hmax} with $N150^\circ \pm 18^\circ$
436 trend. This tectonic field affects Cretaceous carbonates and coincides with the regional
437 tectonic field proposed by [Herraiz et al. \(2000\)](#), [Tavani et al. \(2011\)](#) and [Alcalde et al.](#)
438 [\(2014\)](#).

439

440 *4.2 Late Triassic Outcrop Paleostrain*

441 Strain analysis from HTM5 fault set shows e_y with NW-SE trending and shear regime
442 with extension defined by strike-slip faults (**Fig. 7a**). This is in agreement with the
443 uniaxial extension described in [Tavani \(2012\)](#), constraining this regime with S_{hmin} with
444 NE-SW trending.

445

446 *4.3 Cretaceous Outcrops Paleostrain*

447 We have divided this result in two groups, (a) outcrops within the 20km circle from
448 HPP and (b) the outcrop the HTM17 (**Fig. 5**), which is located in the HPP facilities and
449 described in the next section. HTM14 is the only outcrop from Early Cretaceous age,
450 showing a compressive tectonic stage with reverse fault solutions, defined by e_y with
451 NE-SW trend (**Fig. 7b and 7c**). Taking into account the extensional stage related to the
452 Main Rifting Stage that took place in Early Cretaceous times (i.e. [Carola, 2004](#); [Tavani,](#)
453 [2012](#); [Tugend et al., 2014](#)), we interpreted these results as a modern strain field,
454 probably related to the Cenozoic Inversion stage.

455 Outcrops HTM 2, 3, 8, 17, 19, 20, 21, 22, 23, 25, 26, 29, 31 and 32 are from the upper
456 Cretaceous carbonates (**Fig. 7**). Results are: (1) a compressive strain stage featured by e_y
457 with NW-SE trend, similar to the stage described in [Tavani \(2012\)](#), and (2) a normal

458 strain stage with e_y striking both E-W and NE-SW (**Fig. 7**, HTM 20, 21, 31 and 32).
459 Finally, a (3) shear stage (activated strike-slip faults) and (4) a shear with extension
460 (strike-slip with normal component) were described as well. These two late stages are
461 featured by e_y with NE-SW and NW-SE trends. The existence of four different strain
462 fields is determined by different ages during the Cretaceous and different spatial
463 locations in relation to the main structures, the Ubierna Fault System, Hontomín Fault,
464 Cantabrian Thrust, Montorio folded band and the Polientes syncline (**Fig. 1**).

465

466 *4.4 Cretaceous Outcrop HTM17 on the Hontomín Pilot Plant*

467 This outcrop is located on top of the geological reservoir, in a quarry of Upper
468 Cretaceous limestones. The main advantage of this outcrop is the well-development of
469 striation and carbonate microfibers which yields high-quality data. 105 fault-slip data
470 were measured, with the main orientation striking N75°E; N-50°E; and a conjugate set
471 with N130°E ($\pm 10^\circ$) trend (**Fig. 8**). The result of the strain inversion technique shows an
472 extensional field featured by an e_y trajectory striking N107°E ($\pm 24^\circ$) related to an
473 extensional strain field (see the K' diagram in **figure 8**). Most of the faults are
474 extensional faults NE-SW and NW-SE oriented (**Fig. 9**), in agreement with the
475 extensional RD solution. Reverse faults are oriented NNE-SSW, E-W and WNW-ESE.
476 The advantage of this outcrop is the geographical and stratigraphic position. It is located
477 on top of the HPP facilities in younger sediments than the reservoir rocks. Furthermore,
478 given that the Jurassic reservoir rock and the Cretaceous upper unit are both composed
479 by carbonates, the fault pattern measured here could be a reflex of the fracture network
480 affecting the Jurassic storage rocks in depth (see **Figs. 2, 9**).

481

482 *4.5 Cenozoic outcrops strain field*

483 The Cenozoic tectonic inversion was widely described in the area by different authors
484 (e.g. Carola, 2004; Tavani, 2012; Tungend et al., 2014). This tectonic inversion is
485 related to compressive structures, activating NW-SE and NE-SW thrusts with NW-SE
486 and NNE-SSW e_y trends, respectively. The Ubierna Fault has been inverted with a
487 right-lateral transpressive kinematics during the Cenozoic (Tavani et al., 2011). Early
488 Oligocene outcrop (HTM13, **Figs. 7c**) shows a local extensional field with e_y with
489 NNE-SSW and N150°E trend. During the Lower-Middle Miocene, HTM15 and HTM30
490 outcrops exhibit the same e_y trend, but for a compressive tectonic regime (**Figs. 7d**).
491 HTM1 shows extensional tectonics with e_y oriented N50°E and N130°E. Summarizing,
492 the Cenozoic inversion and tectonic compression are detected during the Early to
493 Middle Miocene and the Oligocene. However, during the middle Miocene only one
494 extensional stage was interpreted (HTM1, **Fig. 7c**).

495 The outcrops located closer to the HPP (HTM 17, 31, 32, **Figs. 5 and 7**) show E-W
496 faults. HTM5 is located on the Ubierna Fault, showing a NW-SE trend, whilst HTM3
497 shows NE-SW strike-slip.

498 Strain analysis suggests that the planes parallel to the S_{Hmax} orientation (NNW-SSE and
499 N-S), could induce the leakage into the reservoir (**Fig. 7**). Moreover, N50°E S_{Hmax}
500 orientation could also affect the reservoir. HPP facilities are close to the Hontomin Fault
501 (**Fig. 5**), a WNW-ESE oriented fault, although the HTM17 station shows that N-S fault
502 planes could play an important role for seepage of fluid into the reservoir.

503

504 5. DISCUSSION

505 5.1 Regional active stress tensor in HTM17 fault pattern

506 The active regional field proposed by Herraiz et al. (2000), Stich et al. (2006), Tavani et
507 al. (2011) and Alcalde et al. (2014), shows e_y , S_{Hmax} with almost NNW-SSE and N-S

508 trends. Namely, the work from Herraiz et al. (2000) calculates three stress tensors
509 within the 20 km of our study area and a Quaternary stress tensor close to the area (c.a.
510 40 km southward of Hontomín). The age of the first one is Miocene, and defined by σ_1
511 $87^\circ/331^\circ$; σ_2 $01^\circ/151^\circ$; σ_3 $00^\circ/061^\circ$ (dip/dip sense 0° - 360°), with an $R=0.06$ and S_{Hmax}
512 trending $N151^\circ E$, under an extensional tectonic regime. Two post-Miocene stress
513 tensors are defined by: (1) σ_1 $87^\circ/299^\circ$; σ_2 $00^\circ/209^\circ$; σ_3 $01^\circ/119^\circ$ with $R = 0.13$, S_{Hmax}
514 with $N29^\circ E$ trend under an extensional tectonic regime and (2) σ_1 $00^\circ/061^\circ$; σ_2
515 $86^\circ/152^\circ$; σ_3 $03^\circ/331^\circ$, with $R=0.76$, and S_{Hmax} $N62^\circ E$ under strike-slip tectonic regime.
516 Finally, these authors calculated a Quaternary stress tensor defined by: σ_1 $85^\circ/183^\circ$; σ_2
517 $02^\circ/273^\circ$; σ_3 $03^\circ/003^\circ$; $R=0.02$ and S_{Hmax} with $N101^\circ E$ trend under an extensional
518 tectonic regime. The regional active stress tensor defined for Pliocene-Quaternary ages
519 is σ_1 $88^\circ/197^\circ$; σ_2 $01^\circ/355^\circ$; σ_3 $00^\circ/085^\circ$ for 327 data with $R = 0.5$ and S_{Hmax} with N-S
520 trend under an extensional tectonic regional regime.

521 We have applied the regional active stress tensor (Herraiz et al., 2000) for studying the
522 reactivation of previous fault patterns measured in HTM17 (Figs. 8 and 9). To carry out
523 this study, we assume that the fault plane reactivation depends on σ_1 and σ_3 , and the
524 shape of the failure envelope. Therefore, we have used the Mohr-Coulomb failure
525 criteria for preexisting fault planes (Xu et al., 2010; Labuz and Zang, 2012), by using
526 the Mohr Plotter v3.0 code (Allmendinger, 2012). Moreover, to calculate the Mohr-
527 Coulomb circle, it is necessary to know the cohesion and friction parameters of the
528 reservoir rock. Bearing in mind that the reservoir rocks are Lower-Jurassic carbonates
529 (dolostone and oolitic limestone, Alcalde et al., 2013, 2014; Ogaya et al., 2013), we
530 have assumed the averaged cohesion for carbonates (limestone and dolostone) in 35°
531 and the coefficient of internal friction of 0.7 (Goodman, 1989). In addition, we have
532 assumed no cohesion with an angle of static friction of 0.7 for preexisting faults.

533 Figure 10 shows the main results for the Mohr analysis. The reactivated planes under
534 the active-present stress field are red dots, 52 out of the original 105 fault-slip
535 measurements at HTM17. Green and orange dots indicate faults with no tectonic
536 strength accumulation under the present-day stress field. Reactivated fault sets are
537 oriented between N to N60°E and N115° to 180°E, with N-S and NNE-SSW as main
538 trends (**Fig. 10**, red rose diagram). Under an extensional tectonic field with $R = 0.5$, N-S
539 are normal faults, whereas NNE-SSW and NNW-SSE trends are strike-slips faults with
540 extensional component. According to the results shown in figure 10, these faults could
541 be reactivated without a pore pressure increase. The inactive fault orientation is
542 constrained between N60°E and N115°E, mainly WNW-ESE (**Fig. 10**, green rose
543 diagram). Regarding the uncertainties of these fault orientations, these values can
544 oscillate $\pm 5^\circ$, according to the field error measurement (averaged error for measuring
545 structures by a compass).

546 Concerning the reliability of the results, some constrains need to be explained. The
547 Mohr-Coulomb failure criterion is an approximation that assumes that the normal stress
548 on the fault plane is not tensile. Furthermore, the increasing of pore pressure in the
549 reservoir rock reduces the normal stress on the plane of failure and the interval of fault
550 reactivation could be higher. This effect was not considered in the previous analysis
551 since the calculation of the critical pore pressure is beyond the purpose of this work.
552 Nevertheless, the MohrPlotter software ([Allmendinger, 2012](#)), allows estimating the
553 increase of pore pressure to the critical value under some conditions.

554 Finally, we have applied the Slip Model and Right Dihedral to the reactivated fault-slip
555 data from HTM17 outcrop (**Fig. 11**), by including the rake estimated from the active
556 regional stress tensor determined by [Herraiz et al. \(2000\)](#). At a glance, faults oriented
557 between N10°E and N10°W act as normal faults (4 out 52, **Figs. 11a, c**), faults between

558 N10°E - N50°E, and N10°W – N50°W act as extensional faults with strike-slip
559 component (31 out 52), and NE-SW and NW-SE vertical faults act as pure strike slips
560 (8 out 52). The Right Dihedral shows a tectonic regime of strike-slip with extensional
561 component (see [De Vicente et al., 1992](#)), with orthorhombic symmetry and S_{Hmax}
562 oriented N10°W, which is in agreement with the stress-tensor proposed by [Herraiz et al.](#)
563 [\(2000\)](#) with $\sigma_2 = 01^\circ/355^\circ$ and σ_1 vertical. However, strain analysis in this case shows
564 a strike-slip extensional tectonic regime, instead of the extensional regime derived from
565 the stress field. Despite this, both the Mohr-Coulomb analysis and the Paleostrain
566 analysis (SM and RD), suggest N-S normal faulting, NNE-SSW to NE-SW and NNW-
567 SSE to NW-SE strike-slips as the active fault network affecting the reservoir. [De](#)
568 [Vicente et al. \(1992\)](#) pointed out that the SM analysis is more robust applied in fault-
569 slip data classified previously by other techniques. Here, we have used the Mohr
570 Coulomb failure criteria to separate active fault set under the same strain tensor,
571 yielding robustness to the results from SM and RD analysis.

572 We propose as a complementary and future work, a combined analysis between the fault
573 population analysis and the slip-tendency analysis ([Morris et al. 1996](#)), which could
574 improve and discriminate those fault sets most likely to be reactivated under an active
575 stress field. Although both analyses (Fault Population and slip-tendency) are based on
576 the stress tensor and the orientation of fault traces, the slip-tendency also includes rock
577 strength values obtained from the "in situ" tests.

578

579 *5.2 Active faulting in the surrounding of HPP*

580 Quaternary tectonic markers for the UFS are suggested by [Tavani et al. \(2011\)](#).
581 According to the tectonic behavior of this fault as right-lateral strike-slip, and the fault
582 segments proposed by [Tavani et al. \(2011\)](#), ranging between 12 and 14 km long, the

583 question is whether this fault could trigger significant earthquakes and which could be
584 the maximum associated magnitude. This is a relevant question given that the “natural
585 seismicity” in the vicinity could affect the integrity of the caprock. Bearing in mind the
586 expectable long-life for the reservoir, estimated in thousands of years, the potential
587 natural earthquake that this master fault could trigger has to be estimated. In this sense,
588 it is necessary to depict seismic scenarios related to large earthquake triggering;
589 however, this type of analysis is beyond the focus of this work.

590 The information that we have to manage in the area of influence (20 km) is: (a)
591 the instrumental seismicity, (b) the geometry of the fault, (c) the total surface rupture,
592 (d) the upper crust thickness and (e) the heat flow across the lithosphere. Starting for the
593 heat flow value, the Hontomín wells show a value that lies between 62 and 78 mW/m²
594 at a 1,500 m depth approximately ([Fernández et al., 1998](#)). Regarding the Moho depth
595 in the area, these aforementioned authors obtained a value ranging between 36 and 40
596 km depth, while the lithosphere base ranges between 120 and 130 km depth ([Torre et
597 al., 2015](#)). The relevance of this value is the study of the thermal weakness into the
598 lithosphere that could nucleate earthquakes in intraplate areas ([Holford et al., 2011](#)). For
599 these authors, the comparison between the crustal heat-flow in particular zones, in
600 contrast with the background regional value, could explain large seismicity and high
601 rates of small earthquakes occurrence, as the case of the New Madrid seismic zone
602 ([Landgraf et al., 2018](#)). For example, in Australia heat-flow values as much as 90
603 mW/m² are related with earthquakes sized $M > 5$ ([Holford et al., 2011](#)).

604 Regarding the maximum expected earthquake into the zone, we have applied the
605 empirical relationships obtained by [Wells and Coppersmith \(1994\)](#). We have used the
606 equations for strike-slip earthquakes according to the strain field obtained in the area
607 (pure shear), and the surface rupture segment for the Ubierna Fault System, assuming a

608 surface rupture segments between 12 and 14 km (Tavani et al., 2011). The obtained
609 results show that the maximum expected earthquake ranges between M 6.0 and M 6.1.
610 Wells and Coppersmith (1994) indicate for these fault parameters a total area rupture
611 ranging between 140 and 150 km². Surface fault traces rupture as lower as 7 km needs
612 at least 20 km of depth in order to reach a value of the fault-area rupturing greater than
613 100 km², in line with a Moho between 36 and 40 in depth.
614 Regarding the instrumental earthquakes recorded into the area, the two largest
615 earthquakes recorded correspond to magnitude M 3.4 and M 3.3, with a depth ranging
616 between 8 and 11 km, respectively, and a felt macroseismic intensity of III (EMS98,
617 www.ign.es, last access on May, 2019). Both earthquakes occurred between 50 and 60
618 km of distance from the Hontomín Pilot Plant. Only five earthquakes have been
619 recorded within the 20-km radius area of influence and with small magnitudes ranging
620 between M 1.5 and M 2.3. The interesting data is the depth of these earthquakes,
621 ranging between 10 and 20 km, which suggest that the seismogenic crust could reach 20
622 km of depth.

623

624 *5.3 Local tectonic field and induced seismicity*

625 The fluid injection into a deep saline aquifer, which is used as GSC, generally increases
626 the pore pressure. The increasing of the pore pressure migrates from the point of
627 injection to the whole reservoir. Moreover, changes into the stress field for faults that
628 are located below the reservoir, could also trigger induced earthquakes (Verdon et al.,
629 2014). Nevertheless, to understand this possibility and the study the volumetric strain
630 field spatial distribution is required (Lisle et al., 2009).

631 We have applied a physic model to estimate the total volume injected (room conditions)
632 and in reservoir conditions. Then we have applied the McGarr's (2014) approximation

633 of the maximum expected seismic moment for induced earthquakes. The injection of 10
634 k tons of CO₂ in Hontomín ([Gastine et al., 2017](#)), represents an approximated injected
635 volume of CO₂ of $5.56 \times 10^6 \text{ m}^3$ (room conditions, pressure of 1 bar and temperature of
636 20 °C). The P/T conditions at the bottom of the wells have a maximum value close to
637 190 bar ([Ortiz et al., 2015](#); [Kovacs et al., 2015](#)), although oscillating between 125 and
638 170 bar and with a maximum temperature close to 58 °C. [Kovacs et al. \(2015\)](#) pointed
639 out a pressure gradient 0.023 MPa/m and a thermal vertical gradient of 0.033 °C/m,
640 which would correspond to a pressure of 357 bar and a temperature of 51 °C at 1,550 m
641 depth. P/T bottom values obtained from the observational wells (HA and HI) by [Ortiz et](#)
642 [al. \(2015\)](#) and [Kovacs et al. \(2015\)](#), were 170 bar and 42 °C respectively.

643 We have used the general law for gases $P_1 \cdot V_1 / T_1 = P_2 \cdot V_2 / T_2$. Therefore, the total
644 injected volume in reservoir conditions according to the parameters observed at the
645 bottom of the wells are, $P_1 = 1.01 \text{ bar}$, $T_1 = 20 \text{ °C}$, $V_1 = 5.56 \times 10^6 \text{ m}^3$, $P_2 = 170 \text{ bar}$ and
646 $T_2 = 42 \text{ °C}$. Hence, the total volume of injected CO₂ plus brine is $6.94 \times 10^4 \text{ m}^3$.

647 [McGarr \(2014\)](#) empirically determined the maximum seismic moment related to a
648 volume increasing by underground injection. The expression is $M_0(\text{max}) \text{ (Nm)} = G \cdot \Delta V$
649 ([McGarr 2014](#), eq. 13), where G is the modulus of rigidity and for the upper limit is $3 \times$
650 10^{10} Pa , and ΔV is the total injected volume (we have used the total injected volume in
651 reservoir conditions). The result is $M_0(\text{max})$ equal to $2.1 \times 10^{15} \text{ Nm}$, which corresponds
652 to a maximum seismic moment magnitude $M_w(\text{max}) = 4.2$, by applying the equation
653 $M_w = (\text{Log } M_0(\text{max}) - 9.05) / 1.5$ from [Hanks and Kanamori \(1979\)](#); where Log is the
654 logarithm to the base 10.

655

656 [McGarr \(2014\)](#) applied this approach for three cases: (1) wastewater injection, (2)
657 hydraulic fracturing, and (3) geothermal injection. We propose to include this approach

658 for fluid injection related to geological storage of CO₂. We assume that the pore
659 pressure increases from CO₂ injection in a similar way that wastewater does (originally
660 defined by [Frohlich, 2012](#)). According to [McGarr \(2014\)](#), the utility of the analysis we
661 have performed is “to predict in advance of a planned injection whether there will be
662 induced seismicity”, and in the case of the HPP, to estimate of the “total injected
663 volume” in a small-scale injection plant.

664 Therefore, the earthquake magnitude to this fluid-injected volume according to the
665 [McGarr \(2014\)](#) and [Verdon et al. \(2014\)](#) could be $M > 4$ if there are faults with a
666 minimum size of 4 km and oriented according to the present-day stress field (N-S
667 extensional faults and NNE-SSW/NNW-SSE strike slip faults; **Fig. 10**). In the case of
668 HPP, there are faults below the reservoir with this potential earthquake triggering
669 ([Alcalde et al., 2014](#)). Also according to [McGarr \(2014\)](#), this value has not to be
670 considered as an absolute physic limit but as a qualitative approximation. Alternatively,
671 increasing by overpressure of the carbonate reservoir along with the pore pressure
672 variations of about 0.5 MPa could trigger earthquakes, as well. Stress-drop related to
673 fluid injections are also reported ([Huang et al., 2016](#)).

674 [Le Gallo and de Dios \(2018\)](#) described two main fault sets affecting the reservoir with
675 N-S and E-W trend, respectively. According to the present-day stress tensor described
676 by [Herraiz et al. \(2000\)](#) and [Tavani et al. \(2011\)](#), E-W fault-sets are accommodating
677 horizontal shortening, which means that the permeability could be low. Besides, these
678 faults are decoupled from the present-day stress tensor. However, N-S faults could act
679 as normal faults and, hence, with higher permeability. In this sense, the study of focal
680 mechanisms solutions could improve the safety management, even for
681 microearthquakes of magnitude lesser than M 3.

682 Moreover, the CO₂ lateral diffusion and pressure variation change during the fluid
683 injection phase, and then the system would relax before to be increased during the next
684 injection phase. In this context, the intermittent and episodic injection of CO₂ could also
685 trigger earthquakes by the stress-field and fluid pressure variations in short time periods.
686

687 6. CONCLUSIONS

688 The application of the analysis for brittle deformation determines the active tectonic
689 strain field, applied in the ongoing seismic monitoring for Geological Carbon Storage
690 (GSC). The possibility that pore pressure variations due to fluid injection could change
691 the stress/strain conditions in the reservoir's caprock, makes the study of the present-
692 day tectonic field as mandatory for the storage safety operations. In this sense, we have
693 to bear in mind that this kind of subsurface storage is designed for long-life expectancy,
694 about thousands of years, and therefore, relevant earthquakes could occur affecting the
695 sealing and the seepage of CO₂, compromising the integrity of the reservoir. Hence, we
696 can conclude from our analysis the following items:

697 (1) The study of the tectonic field allows classifying the geometry of the faults to
698 prevent prone earthquake-related structures and design monitoring seismic network.

699 (2) The influence area around the facilities of the GSC for studying the active
700 stress/strain field could reach 20 km from the facility, adding missing information from
701 map scale and boreholes. This information could be used from the 3D local fracture
702 pattern estimation to avoid the pore overpressure. Analysis of the stress-drop due to the
703 fluid injection could be combined with this information to understand potential
704 microseismicity associated with the injection operations.

705 (3) In the case of Hontomín Pilot-Plant, we have obtained two strain active tectonic
706 fields featured as shear deformation. These fields are defined by (a) a local tectonic

707 strain field with e_y , S_{Hmax} striking N50°E and (b) the regional one defined by e_y , S_{Hmax}
708 with N150°E trend. In this context, strike-slip faults with N-S, NNE-SSW and NNW-
709 SSE trends, are accumulating present-day tectonic deformation. Analysis of Mohr-
710 Coulomb failure criterion shows a potential reactivation of these fault sets.

711 (4) N-S faults are accumulating tectonic deformation and they could act as normal
712 faults. This means that this fault set is the preferential direction for potential fluid
713 leakage. In addition, intersection with NNE-SSW and NNW-SSE could arrange 3D
714 networks for fluid mobilization and leakage.

715 (5) The Ubierna Fault System represents a tectonically active fault array that could
716 trigger natural earthquakes as large as M 6 (± 0.1), from the empirical relationship of the
717 total rupture segment (ranging between 12 and 14 km, and the total fault-area rupture,
718 oscillating between 100 and 150 km²). Despite the lack of instrumental seismicity into
719 the influence area, we cannot obviate the potential earthquake occurrence within
720 intraplate areas due to the long- timescale expected-life of the GSC. The heat-flow
721 values and thermal crust conditions could determine the presence of intraplate
722 earthquakes with magnitude $M > 5$, for a long timescale (thousands of years), and the
723 total injected fluid could trigger induced earthquakes greater than M 4.

724 The active strain field is now defined by an extensional tectonic defined by e_y with N-S
725 trend, activating N-S normal faults and right-lateral faults with NNW- and NNE- trends.
726 Finally, we state that the determination of the active tectonic strain field, the application
727 of the slip-tendency analysis, the recognition and study of active faults within the area
728 of influence (20 km), the estimation of the maximum potential triggered natural
729 earthquake, the modeling of the stress-change during the fluid injection and stress-drop,
730 probably improve the operations for a secure storage. In a short future, earthquake

731 scenarios will be the next step: modeling the Coulomb static stress-changes due to fluid

732 injection and the modeling of intensity maps of horizontal seismic acceleration.

733

734 ACKNOWLEDGEMENTS

735 Thanks are given to Pr. Graham Yielding, Dr. Dave Haley, and an anonymous reviewer
736 for their remarks during the open discussion. We wish to thank Pr. Allmendinger for the
737 free use of the MohrPlotter 3.0 software, last access in March of 2020 at the web
738 browser: <http://www.geo.cornell.edu/geology/faculty/RWA/programs/mohrplotter.html>

739 This work has been partially supported by the European Project ENOS: ENabling
740 Onshore CO₂ Storage in Europe, H2020 Project ID: 653718 and the Spanish project
741 3GEO, CGL2017-83931-C3-2-P, MICIU-FEDER. The authors would also thank the
742 crew of CIUDEN at Hontomín facilities for their kind assistance during our fieldwork.

743

744 REFERENCES

- 745 Alcalde, J., Martí, D., Calahorrano, A., Marzan, I., Ayarza, P., Carbonell, R., Juhlin, C.,
746 and Pérez-Estaún, A.: Active seismic characterization experiments of the Hontomín
747 research facility for geological storage of CO₂, Spain, *Int. J. Greenh. Gas Con.*, 19,
748 785–795, <http://dx.doi.org/10.1016/j.ijggc.2013.01.039>, 2013.
- 749 Alcalde J., Marzán I., Saura E., Martí D., Ayarza P., Juhlin C., Pérez-Estaún, A., and
750 Carbonell, R.: 3D geological characterization of the Hontomín CO₂ storage site,
751 Spain: Multidisciplinary approach from seismic, well-log and regional data,
752 *Tectonophysics*, 627, 6–25, <http://dx.doi.org/10.1016/j.tecto.2014.04.025>, 2014.
- 753 Allmendinger, R. W., Cardozo, N. C., and Fisher, D.: *Structural Geology Algorithms:
754 Vectors & Tensors*, Cambridge, England, Cambridge University Press, 289 pp, 2012.
- 755 Álvarez-Gómez, J. A.: FMC: a one-liner python program to manage, classify and plot
756 focal mechanisms, EGU General Assembly, Vienna, Austria, 27 April-02 May,
757 EGU2014-10887, 2014.
- 758 Anderson, E. M.: *The Dynamics of Faulting and Dyke Formation with application to
759 Britain*, 2nd ed., Oliver and Boyd, Edinburgh, 206 pp., 1951.
- 760 Angelier, J.: Determination of the mean principal directions of stresses for a given fault
761 population, *Tectonophysics*, 56, 17-26, [https://doi.org/10.1016/0040-1951\(79\)90081-](https://doi.org/10.1016/0040-1951(79)90081-7)
762 [7](https://doi.org/10.1016/0040-1951(79)90081-7), 1979.
- 763 Angelier, J.: Tectonic analysis of fault slip data sets, *J. Geophys. Res.*, 89, 5835-5848,
764 <https://doi.org/10.1029/JB089iB07p05835>, 1984.
- 765 Angelier, J.: Inversion of field data in fault tectonics to obtain the regional stress-III. A
766 new rapid direct inversion method by analytical means, *Geophys. J. Int.*, 103, 363-
767 376, <https://doi.org/10.1111/j.1365-246X.1990.tb01777.x>, 1990.
- 768 Angelier, J. and Mechler, P.: Sur une méthode graphique de recherche des contraintes
769 principales également utilisable en tectonique et en séismologie: la méthode des
770 dièdres droits, *B. Soc. Geol. Fr.*, 19, 1309-1318,
771 <http://dx.doi.org/10.2113/gssgfbull.S7-XIX.6.1309>, 1977.
- 772 Aurell, M., Meléndez, G., Olóriz, F., Bádenas, B., Caracuel, J. E., García-Ramos, J. C.,
773 Goy, A., Linares, A., Quesada, S. and Robles, S.: Jurassic, in *The geology of Spain*,
774 pp. 213–253, The Geological Society of London., 2002.
- 775 Bentham, M. and Kirby, G.: CO₂ Storage in Saline Aquifers. *Oil Gas Sci. Technol.*, 60,
776 559-567, <https://doi.org/10.2516/ogst:2005038>, 2005.

- 777 Bott, M.H.P.: The mechanism of oblique-slip faulting, *Geol. Mag.*, 96: 109-117.
778 <https://doi.org/10.1017/S0016756800059987>, 1959.
- 779 Capote, R., De Vicente, G., and González Casado, J. M.: An application of the slip
780 model of brittle deformation to focal mechanism analysis in three different plate
781 tectonics situation. *Tectonophysics*, 191, 399-409, [https://doi.org/10.1016/0040-](https://doi.org/10.1016/0040-1951(91)90070-9)
782 [1951\(91\)90070-9](https://doi.org/10.1016/0040-1951(91)90070-9), 1991.
- 783 Calvet, F., Anglada, E. and Salvany, J. M.: El Triásico de los Pirineos, in Vera, J.A.
784 (ed.) *Geología de España*, pp. 272–274, SGE–IGME, Madrid, 2004.
- 785 Carola, E.: The transition between thin-to-thick-skinned styles of deformation in the
786 Western Pyrenean Belt. Ph. D. thesis, Universitat de Barcelona, 271 pp., 2004.
- 787 Christensen, N. P.: Report on the current state and need for further research on CO₂
788 capture and storage. CO2NET, European Carbon Dioxide Network,
789 www.co2net.com, 2004.
- 790 Chu, S.: Carbon Capture and Sequestration, *Science*, 325, 1599,
791 <http://dx.doi.org/10.1126/science.1181637>, 2009.
- 792 Dallmeyer, R. D. and Martínez-García, E., Eds.: *Pre-Mesozoic Geology of Iberia*,
793 Springer-Verlag, Berlin Heidelberg, 1990.
- 794 De Vicente, G.: Análisis Poblacional de Fallas. El sector de enlace Sistema Central-
795 Cordillera Ibérica. Ph. D. thesis, Universidad Complutense de Madrid, Spain, 317
796 pp., 1988.
- 797 De Vicente, G. Muñoz, A., Giner, J.L.: Use of the Right Dihedral Method: implications
798 from the Slip Model of Fault Population Analysis, *Rev. Soc. Geol. España*, 5(3-4), 7-
799 19. 1992.
- 800 De Vicente, G., Cloetingh, S., Muñoz-Martín, A., Olaiz, A., Stich, D., Vegas, R.,
801 Galindo-Zaldívar, J., and Fernández-Lozano, J.: Inversion of moment tensor focal
802 mechanisms for active stresses around Microcontinent Iberia: Tectonic implications,
803 *Tectonics*, 27: 1-22, <http://dx.doi.org/10.1029/2006TC002093>, 2008.
- 804 De Vicente, G., Cloetingh, S., Van Wees, J. D., and Cunha, P. P.: Tectonic
805 classification of Cenozoic Iberian foreland basins, *Tectonophysics*, 502, 38–61,
806 <http://dx.doi.org/10.1016/j.tecto.2011.02.007>, 2011.
- 807 Etchecopar, A., Vasseur, G., and Daignieres, M.: An inverse problem in microtectonics
808 for the determination of stress tensor from fault striation analysis, *J. Struct. Geol.*, 3,
809 51-65, [http://dx.doi.org/10.1016/0191-8141\(81\)90056-0](http://dx.doi.org/10.1016/0191-8141(81)90056-0), 1981.

- 810 Fernández, M., Marzán, I., Correia, A., and Ramalho, E.: Heat flow, heat production,
811 and lithospheric thermal regime in the Iberian Peninsula, *Tectonophysics*, 291, 29-
812 53, [http://dx.doi.org/10.1016/S0040-1951\(98\)00029-8](http://dx.doi.org/10.1016/S0040-1951(98)00029-8), 1998.
- 813 Foulger, G. R., Wilson, M., Gluyas, J., Julian, B. R. and Davies, R.: Global review of
814 human-induced earthquakes, *Earth-Sci. Rev.*, 178, 438–514,
815 <http://dx.doi.org/10.1016/j.earscirev.2017.07.008>, 2018.
- 816 Frohlich, C.: Two-year survey comparing earthquake activity and injection-well
817 locations in the Barnett Shale, Texas. *PNAS*, vol. 109 (35), 13934 – 13938,
818 <https://doi.org/10.1073/pnas.1207728109>, 2012.
- 819 García-Mondéjar, J., Pujalte, V. and Robles, S.: Características sedimentológicas,
820 secuenciales y tectoestratigráficas del Triásico de Cantabria y norte de Palencia,
821 *Cuad. Geol. Ibérica*, (10), 151–172, 1986.
- 822 García-Mondéjar, J., Agirrezabala, L. M., Aranburu, A., Fernández-Mendiola, P. A.,
823 Gómez-Pérez, I., López-Horgue, M. and Rosales, I.: Aptian-Albian tectonic pattern
824 of the Basque-Cantabrian Basin (Northern Spain), *Geological Journal*, 31(1), 13–45,
825 [http://dx.doi.org/10.1002/\(SICI\)1099-1034\(199603\)31:1<13::AID-GJ689>3.0.CO;2-](http://dx.doi.org/10.1002/(SICI)1099-1034(199603)31:1<13::AID-GJ689>3.0.CO;2-Y)
826 [Y](http://dx.doi.org/10.1002/(SICI)1099-1034(199603)31:1<13::AID-GJ689>3.0.CO;2-Y), 1996.
- 827 Gastine, M., Berenblyum, R., Czernichowski-lauriol, I., de Dios, J. C., Audigane, P.,
828 Hladik, V., Poulsen, N., Vercelli, S., Vincent, C., and Wildenborg, T.: Enabling
829 onshore CO₂ storage in Europe: fostering international cooperation around pilot and
830 test sites, *Energy Proced.*, 114, 5905–5915,
831 <http://dx.doi.org/10.1016/j.egypro.2017.03.1728>, 2017.
- 832 Giner-Robles, J.L., Pérez-López, R., Elez, J., Silva, P.G., Rodríguez Escudero, E.,
833 Canora, C., Rodríguez-Pascua, M.A., Bardají, T., Roquero, E., Huerta, P., Perucha,
834 M.A.: Strain analysis in the Iberian Peninsula from focal mechanism solutions,
835 seismic hazard impacts, In: C. Canora, F. Martín, E. Masana, R. Pérez y M. Ortuño,
836 Eds., pp. 249-252. Tercera reunión ibérica sobre fallas activas y paleosismología,
837 Alicante (España), 2018.
- 838 Goldberg, D. S., Kent, D. V., and Olsen, P. E.: Potential on-shore and off-shore
839 reservoirs for CO₂ sequestration in Central Atlantic magmatic province basalts, P.
840 *Natl. Acad. Sci. USA*, 107, 1327–1332, <http://dx.doi.org/10.1073/pnas.0913721107>,
841 2010.

- 842 Gómez, M., Vergés, J. and Riaza, C.: Inversion tectonics of the northern margin of the
843 Basque Cantabrian Basin, *Bulletin de la Société Géologique de France*, 173(5), 449–
844 459, <http://dx.doi.org/10.2113/173.5.449>, 2002.
- 845 Goodman, R. E.: *Introduction to Rock Mechanics*, 2nd Edition, John Wiley & Sons, Inc.,
846 New York. 576 pp., 1989.
- 847 Hanks, T.C., Kanamori, H.: A Moment Magnitude Scale, *J. Geophys. Res.*, 84 (B5),
848 2348–2350, <https://doi.org/10.1029/JB084iB05p02348>, 1979.
- 849 Herraiz, M., De Vicente, G., Lindo-Naupari, R., Giner, J., Simón, J.L., González-
850 Casado, J.M., Vadillo, O., Rodríguez-Pascua, M.A., Cicuéndez, J.I., Casas, A.,
851 Cabañas, L., Rincón, P., Cortés, A.L., Ramírez, M., and Lucini, M.: The recent
852 (upper Miocene to Quaternary) and present tectonic stress distributions in the Iberian
853 Peninsula, *Tectonics*, 19, 762–786, <https://doi.org/10.1029/2000TC900006>, 2000.
- 854 Holford, S. M., Hillis, R. R., Hand, M., and Sandiford, M.: Thermal weakening
855 localizes intraplate deformation along the southern Australian continental margin,
856 *Earth Planet. Sc. Lett.*, 305, 207–214, <http://dx.doi.org/10.1016/j.epsl.2011.02.056>,
857 2011.
- 858 Huang, Y., Beroza, G. C., and Ellsworth, W. L.: Stress drop estimates of potentially
859 induced earthquakes in the Guy-Greenbrier sequence, *J. Geophys. Res.-Sol. Ea.*, 121,
860 6597–6607, <http://dx.doi.org/10.1002/2016JB013067>, 2016.
- 861 Kaverina, A. N., Lander, A. V., and Prozorov, A. G.: Global creepex distribution and its
862 relation to earthquake-source geometry and tectonic origin, *Geophys. J. Int.*, 125,
863 249-265, <https://doi.org/10.1111/j.1365-246X.1996.tb06549.x>, 1996.
- 864 Kovacs, T., Poulussen, D.F. and de Dios, C.: Strategies for injection of CO₂ into
865 carbonate rocks at Hontomin. Final Technical Report, Global Carbon Capture and
866 Storage Institute Ltd. 2015. 66p.
867 [https://www.globalccsinstitute.com/archive/hub/publications/193428/strategies-](https://www.globalccsinstitute.com/archive/hub/publications/193428/strategies-injection-co2-carbonate-rocks-hontomin-final-technical-report.pdf)
868 [injection-co2-carbonate-rocks-hontomin-final-technical-report.pdf](https://www.globalccsinstitute.com/archive/hub/publications/193428/strategies-injection-co2-carbonate-rocks-hontomin-final-technical-report.pdf), 2015.
- 869 Labuz, J. F., Zang, A.: Mohr–Coulomb Failure Criterion. *Rock Mech. Rock Eng.*, 45,
870 975–979, <https://doi.org/10.1007/s00603-012-0281-7>, 2012.
- 871 Landgraf, A., Kuebler, S., Hintersberger, E., Stein, S.: Active tectonics, earthquakes and
872 palaeoseismicity in slowly deforming continents, Landgraf, A., Kuebler, S.,
873 Hintersberger, E. & Stein, S. (eds) *Seismicity, Fault Rupture and Earthquake*
874 *Hazards in Slowly Deforming Regions*. Geological Society, London, Special
875 Publications, 432, <http://doi.org/10.1144/SP432.13>, 2018.

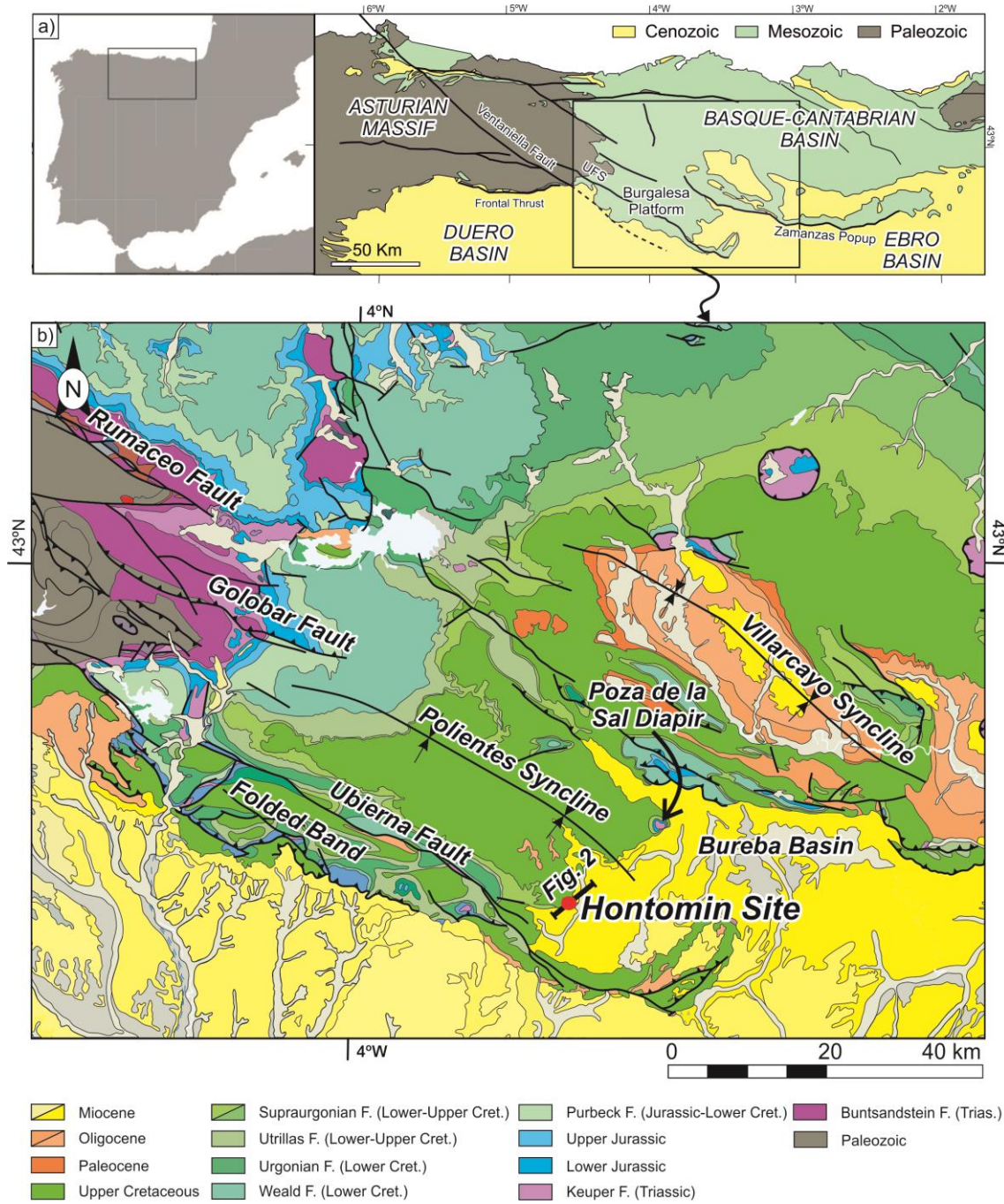
- 876 Le Gallo, Y. and de Dios, J. C.: Geological Model of a Storage Complex for a CO₂
877 Storage Operation in a Naturally-Fractured Carbonate Formation, *Geosciences*, 2018,
878 8, 354, <http://dx.doi.org/10.3390/geosciences8090354>, 2018.
- 879 Le Pichon, X. and Sibuet, J.-C.: Western extension of boundary between European and
880 Iberian plates during the Pyrenean orogeny, *Earth and Planetary Science Letters*,
881 12(1), 83–88, [http://dx.doi.org/10.1016/0012-821X\(71\)90058-6](http://dx.doi.org/10.1016/0012-821X(71)90058-6), 1971.
- 882 Lepvrier, C. and Martínez-García, E.: Fault development and stress evolution of the
883 post-Hercynian Asturian Basin (Asturias and Cantabria, northwestern Spain),
884 *Tectonophysics*, 184, 345, [http://dx.doi.org/10.1016/0040-1951\(90\)90447-G](http://dx.doi.org/10.1016/0040-1951(90)90447-G), 1990.
- 885 Lisle, R. J., Aller, J., Bastida, F., Bobillo-Ares, N. C., and Toimil, N. C.: Volumetric
886 strains in neutral surface folding, *Terra Nova*, 21, 14–20,
887 <http://dx.doi.org/10.1111/j.1365-3121.2008.00846.x>, 2009.
- 888 McGarr, A.: Maximum magnitude earthquakes induced by fluid injection, *J. Geophys.*
889 *Res.*, 119, 1008–1019, <https://doi.org/10.1002/2013JB010597>, 2014.
- 890 McNamara, D.D. Methods and techniques employed to monitor induced seismicity
891 from carbon capture and storage, GNS Science Report 2015/18, 23 pp.,
892 <http://dx.doi.org/10.13140/RG.2.2.13830.98888>, 2016.
- 893 Morris, A., Ferrill, D. A. and Henderson, D. B.: Slip-tendency analysis and fault
894 reactivation, *Geology*, 24, 275-278, [http://doi.org/10.1130/0091-7613\(1996\)024<0275:STAAFR>2.3.CO;2](http://doi.org/10.1130/0091-7613(1996)024<0275:STAAFR>2.3.CO;2), 1996.
- 896 Muñoz, J. A.: Evolution of a continental collision belt: ECORS-Pyrenees crustal
897 balanced cross-section, in *Thrust Tectonics*, edited by K. R. McClay, pp. 235–246,
898 Springer Netherlands, Dordrecht., 1992.
- 899 Ogaya, X., Ledo J., Queralt P., Marcuello, A., and Quintà, A.: First geoelectrical image
900 of the subsurface of the Hontomín site (Spain) for CO₂ geological storage: A
901 magnetotelluric 2D characterization, *Int. J. Greenh. Gas Con.*, 13, 168–179,
902 <https://dx.doi.org/10.1016/j.ijggc.2012.12.023>, 2013.
- 903 Orr, F.M.: Onshore Geologic Storage of CO₂, *Science*, 325, 1656-1658,
904 <http://dx.doi.org/10.1126/science.1175677>, 2009.
- 905 Ortiz, G., Kovacs, T., Poulussen, D.F. and de Dios, C.: Hontomin reservoir
906 characterisation test, Final Technical Report. Global Carbon Capture and Storage
907 Institute Ltd. 2015. 48p. <https://www.globalccsinstitute.com/resources/publications-reports-research/?filter=2015-05-01,2015-07-25&type=date>, 2015.

- 909 Pan, P., Wu, Z., Feng, X., Yan, F.: Geomechanical modeling of CO₂ geological storage:
910 A review, *J. Rock Mech. and Geotech. Eng.*, 8, 936-947,
911 <http://dx.doi.org/10.1016/j.jrmge.2016.10.002>, 2016.
- 912 Pérez-López, R., Mediato, J.F., Rodríguez-Pascua, M.A., Giner-Robles, J.L., Martínez-
913 Orío, R., Arenillas-González, A., Fernández-Canteli, P., de Dios, J.C., Loubeau, L.:
914 Aplicación del análisis estructural y campos de deformación para el estudio de
915 sismicidad inducida en almacenamiento profundo: Hontomín, In: C. Canora, F.
916 Martín, E. Masana, R. Pérez y M. Ortuño, Eds., pp. 279-282. Tercera reunión ibérica
917 sobre fallas activas y paleosismología, Alicante (España), 2018.
- 918 Pearce, J. M.: What can we learn from Natural Analogues? An overview of how
919 analogues can benefit the geological storage of CO₂, in: *Advances in the Geological*
920 *Storage of Carbon Dioxide*, edited by: Lombardi, S., Altunina, L. K., and Beaubien,
921 S. E., Springer, Dordrecht, The Netherlands, 129–139, 2005.
- 922 Pegoraro, O.: Application de la microtectonique à un étude de neotectonique. Le golfe
923 Maliaque (Grèce centrale). Ph.D. thesis, U.S.T.L. Montpellier, France, 41 pp., 1972.
- 924 Permentier, K., Vercammen, S., Soetaert, S., and Schellemans, Ch.: Carbon dioxide
925 poisoning: a literature review of an often forgotten cause of intoxication in the
926 emergency department, *International Journal of Emergency Medicine*, 10, 14,
927 <http://dx.doi.org/10.1186/s12245-017-0142-y>, 2017.
- 928 Quintà, A. and Tavani S., The foreland deformation in the south-western Basque–
929 Cantabrian Belt (Spain), *Tectonophysics*, 576–577, 4–19,
930 <http://dx.doi.org/10.1016/j.tecto.2012.02.015>, 2012.
- 931 Reches, Z.: Faulting of rocks in three-dimensional strain fields, II. Theoretical analysis,
932 *Tectonophysics*, 95, 133-156, [https://doi.org/10.1016/0040-1951\(83\)90264-0](https://doi.org/10.1016/0040-1951(83)90264-0), 1983.
- 933 Reches, Z.: Determination of the tectonic stress tensor from slip along faults that obey
934 the Coulomb yield condition, *Tectonics*, 7, 849-861,
935 <https://doi.org/10.1029/TC006i006p00849>, 1987.
- 936 Rice, S. A.: Health effects of acute and prolonged CO₂ exposure in normal and sensitive
937 populations, Second Annual Conference on Carbon Sequestration, Alexandria,
938 Virginia, USA, 5-6 May, 2003.
- 939 Roca, E., Muñoz, J. A., Ferrer, O. and Ellouz, N.: The role of the Bay of Biscay
940 Mesozoic extensional structure in the configuration of the Pyrenean orogen:
941 Constraints from the MARCONI deep seismic reflection survey, *Tectonics*, 30(2),
942 <https://10.1029/2010TC002735>, 2011.

- 943 Röhmann, L., Tillner, E., Magri, F., Kühn, M., and Kempka, T.: Fault reactivation and
944 ground surface uplift assessment at a prospective German CO₂ storage site, Energy
945 *Proced.*, 40, 437–446. <http://dx.doi.org/10.1016/j.egypro.2013.08.050>, 2013.
- 946 Scholz, C.: The seismic cycle. In *The Mechanics of Earthquakes and Faulting* 3rd
947 edition, Cambridge, Cambridge University Press, pp. 228-277, 2018.
- 948 Serrano, A. and Martínez del Olmo, W.: Tectónica salina en el Dominio Cantabro–
949 Navarro: evolución, edad y origen de las estructuras salinas, in: *Formaciones*
950 *evaporíticas de la Cuenca del Ebro y cadenas periféricas, y de la zona de Levante*,
951 edited by: Orti, F. and Salvany, J.M., Empresa Nacional De Residuos Radiactivos
952 S.A, ENRESA-GPPG, Barcelona, Spain, 39–53, 1990.
- 953 Simpson, R. S.: Quantifying Anderson's fault types, *J. Geophys. Res.*, 102, 17,909–
954 17,919, <https://doi.org/10.1029/97JB01274>, 1997.
- 955 Stich, D., Serpelloni, E., Mancilla, F. L., and Morales, J.: Kinematics of the Iberia–
956 Maghreb plate contact from seismic moment tensors and GPS observations,
957 *Tectonophysics*, 426, 295-317. <https://doi.org/10.1016/j.tecto.2006.08.004>, 2006.
- 958 Soto R., Casa-Sainz A. M., and Villalaín, J. J.: Widespread Cretaceous inversion event
959 in northern Spain: evidence from subsurface and palaeomagnetic data, *Journal of the*
960 *Geological Society London*, 168, 899-912, [http://dx.doi.org/10.1144/0016-](http://dx.doi.org/10.1144/0016-76492010-072)
961 [76492010-072](http://dx.doi.org/10.1144/0016-76492010-072), 2011.
- 962 Tavani, S., Quintá, A., and Granado, P.: Cenozoic right-lateral wrench tectonics in the
963 Western Pyrenees (Spain): The Ubierna Fault System, *Tectonophysics*, 509, 238–
964 253, <http://dx.doi.org/10.1016/j.tecto.2011.06.013>, 2011.
- 965 Tavani, S.: Plate kinematics in the Cantabrian domain of the Pyrenean orogeny, *Solid*
966 *Earth*, 3, 265–292, <http://dx.doi.org/10.5194/se-3-265-2012>, 2012.
- 967 Tavani, S., Carola, C., Granado, P., Quintà, A., and Muñoz, J. A.: Transpressive
968 inversion of a Mesozoic extensional forced fold system with an intermediate
969 décollement level in the Basque - Cantabrian Basin (Spain), *Tectonics*, 32,
970 <http://dx.doi.org/10.1002/tect.20019>, 2013.
- 971 Torne, M., Fernández, M., Vergés, J., Ayala, C., Salas, M. C., Jimenez-Munt, I.,
972 Buffett, G. G., and Díaz, J.: Crust and mantle lithospheric structure of the Iberian
973 Peninsula deduced from potential field modeling and thermal analysis,
974 *Tectonophysics*, 663, 419–433, <http://dx.doi.org/10.1016/j.tecto.2015.06.003>, 2015.
- 975 Tugend, J., Manatschal, G., Kusznir, N. J., Masini, E., Mohn, G. and Thion, I.:
976 Formation and deformation of hyperextended rift systems: Insights from rift domain

- 977 mapping in the Bay of Biscay-Pyrenees, *Tectonics*, 33(7), 1239–1276,
978 <http://dx.doi.org/10.1002/2014TC003529>, 2014.
- 979 Vegas, R., Vázquez, J. T., Olaiz, A. J., and Medialdea, T.: Tectonic model for the latest
980 Triassic - Early Jurassic extensional event in and around the Iberian Peninsula,
981 *Geogaceta*, 60, 23-26, 2016.
- 982 Verdon, J. P.: Significance for secure CO₂ storage of earthquakes induced by fluid
983 injection, *Environ. Res. Lett.*, 9, 064022 (10pp), <http://dx.doi.org/10.1088/1748-9326/9/6/064022>, 2014.
- 985 Verdon, J. P., Stork, A. L., Bissell, R. C., Bond, C. E., and Werner, M. J.: Simulation of
986 seismic events induced by CO₂ injection at In Salah, Algeria, *Earth Planet. Sci. Lett.*,
987 426, 118–129, <http://dx.doi.org/10.1016/j.epsl.2015.06.029>, 2015.
- 988 Vergés, J., Fernández, M. and Martínez, A.: The Pyrenean orogen: pre-, syn-, and post-
989 collisional evolution, *J. Virt. Ex.*, 08,
990 <http://dx.doi.org/10.3809/jvirtex.2002.00058>, 2002.
- 991 Wells, D. L. and Coppersmith, K. J.: New empirical relationships among magnitude,
992 rupture length, rupture width, rupture area, and surface displacement, *B. Seismol.*
993 *Soc. Am.*, 84, 974–1002, 1994.
- 994 Wilson, M. P., Foulger, G. R., Gluyas, J. G., Davies, R. J., and Julian, B. R.: HiQuake
995 the human-induced earthquake database, *Seismol. Res. Lett.*, 88, 1560-1565,
996 <http://dx.doi.org/10.1785/0220170112>, 2017.
- 997 Winthaegen, P., Arts, R., and Schroot, B.: Monitoring Subsurface CO₂ Storage. *Oil Gas*
998 *Sci. Technol.*, 60, 573-582, 2005.
- 999 Xu, S.-S., A.F. Nieto-Samaniego, S.A. Alaniz-Álvarez: 3D Mohr diagram to explain
1000 reactivation of pre-existing planes due to changes in applied stresses, *Rock Stress*
1001 *and Earthquakes – Xie (ed.)*, 739-745 p, 2010.
- 1002 Žalohar, J. and Vrabec, M.: Combined kinematic and paleostress analysis of fault-slip
1003 data: The Multiple-slip method, *J. Struct. Geol.*, 30, 1603–1613,
1004 <http://dx.doi.org/10.1016/j.jsg.2008.09.004>, 2008.
- 1005

1006 **FIGURE CAPTIONS**



1007

1008

1009

1010

1011

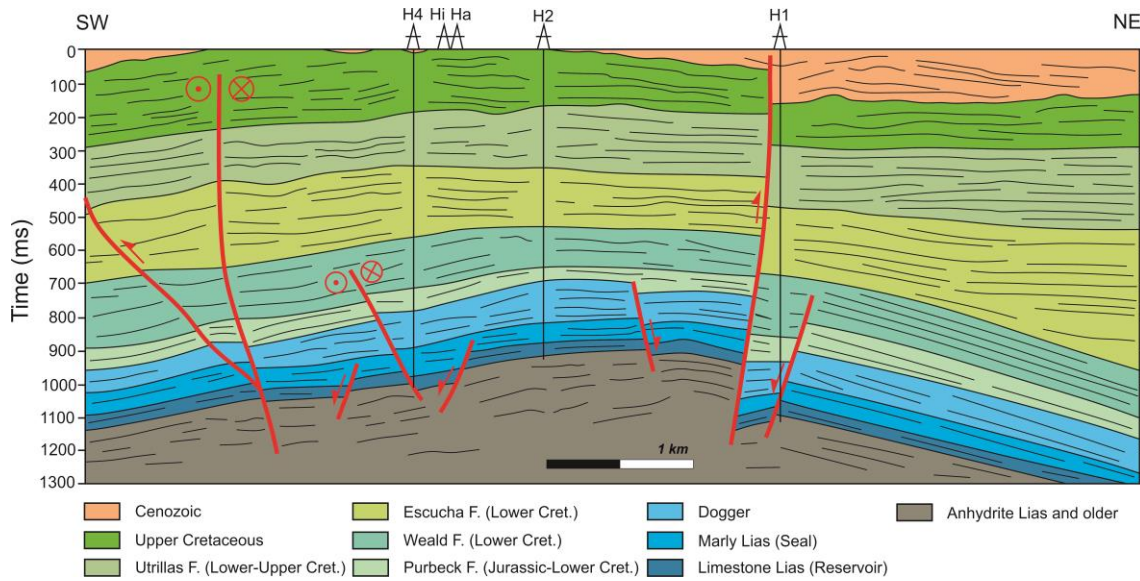
1012

1013

1014

1015

Figure 1. a) Location map of the study area in the Iberian Peninsula, along with the geological map of the Asturian and Basque-Cantabrian areas, labelling major units and faults (modified after Quintà and Tavani 2012); b) Geographical location of Hontomín pilot-plant (red dot) within the Basque-Cantabrian Basin. This basin is tectonically controlled by the Ubierna Fault System (UFS; NW-SE oriented) and the parallel Polientes syncline, the Duero and Ebro Tertiary basins and Poza de la Sal evaporitic diapir. Cret: Cretaceous; F: Facies.

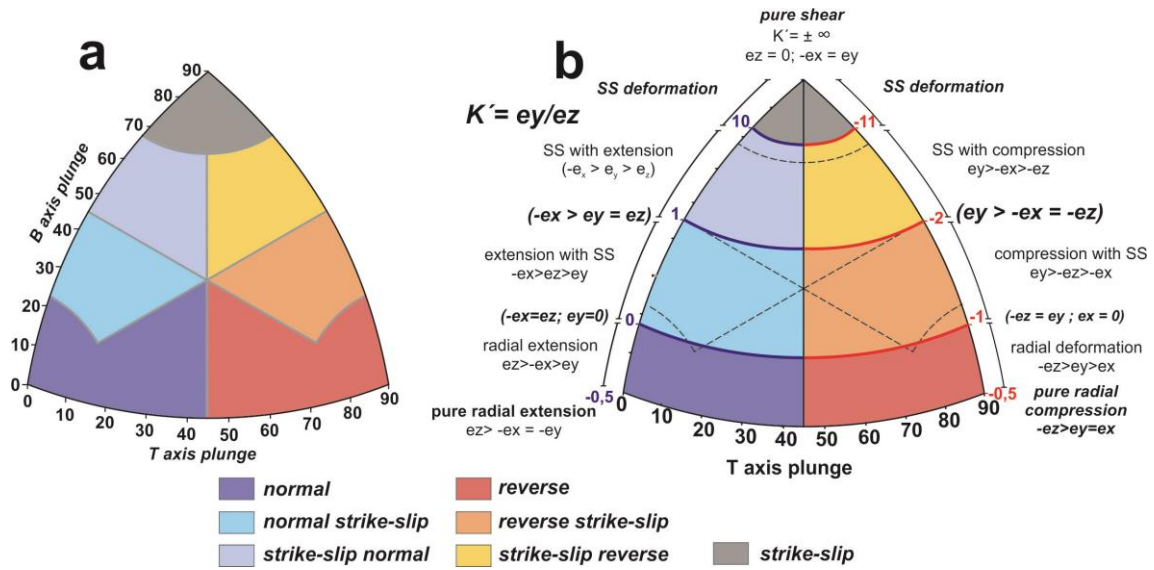


1016

1017

1018 **Figure 2.** Interpretation of a 2D seismic reflection profile crossing the oil exploration
1019 wells (H1, H2 and H4), along with the monitoring well (Ha) and injection well (Hi)
1020 through Hontomin Pilot Plant (HPP). Modified from Alcalde et al. (2014). See Figure 1
1021 for location, black line at the red circle.

1022



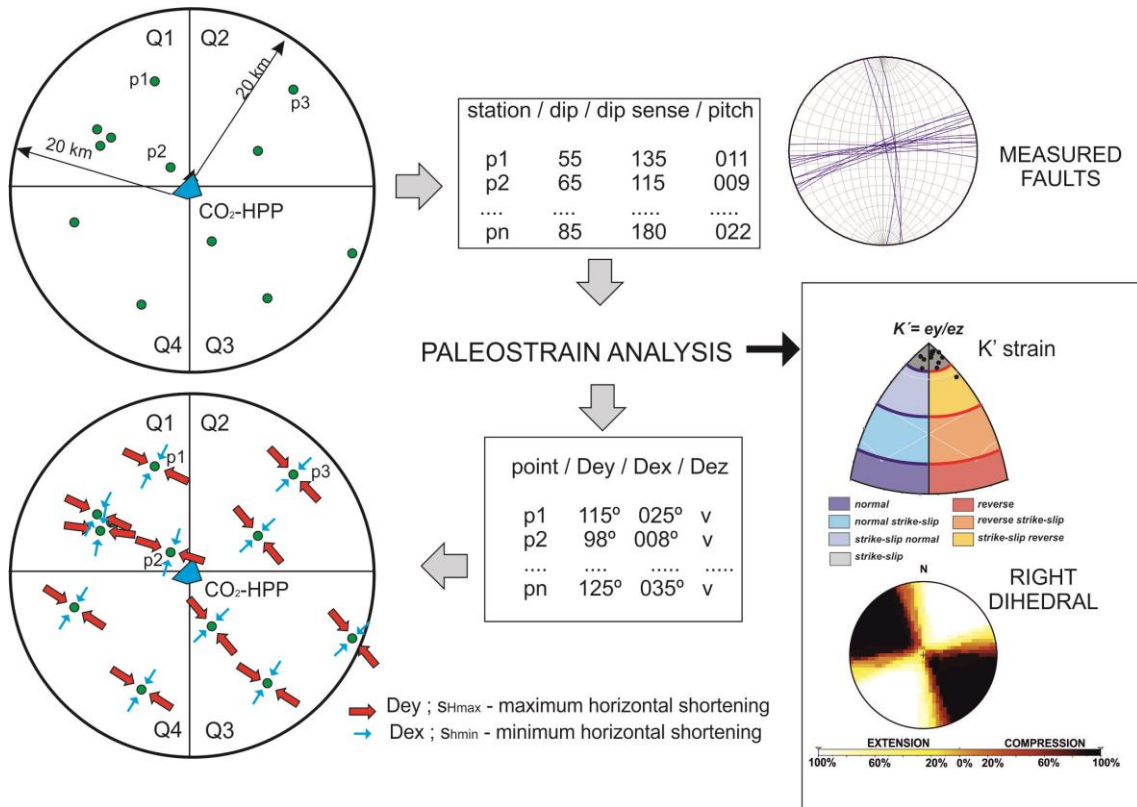
1023

1024

1025 **Figure 3.** a) Kaverina original diagram to represent the tectonic regime from an
 1026 earthquake focal mechanism population (see Kaverina et al., 1996 and Álvarez-Gómez,
 1027 2014). b) K' -strain diagram used in this work. Dotted lines represent the original
 1028 Kaverina limits. Colored zones represent the type of fault. The tectonic regime is also
 1029 indicated by the relationship between the strain axes and the colored legend. SS Strike
 1030 slip. The B axis is the orthogonal to the P and T axes.

1031

1032

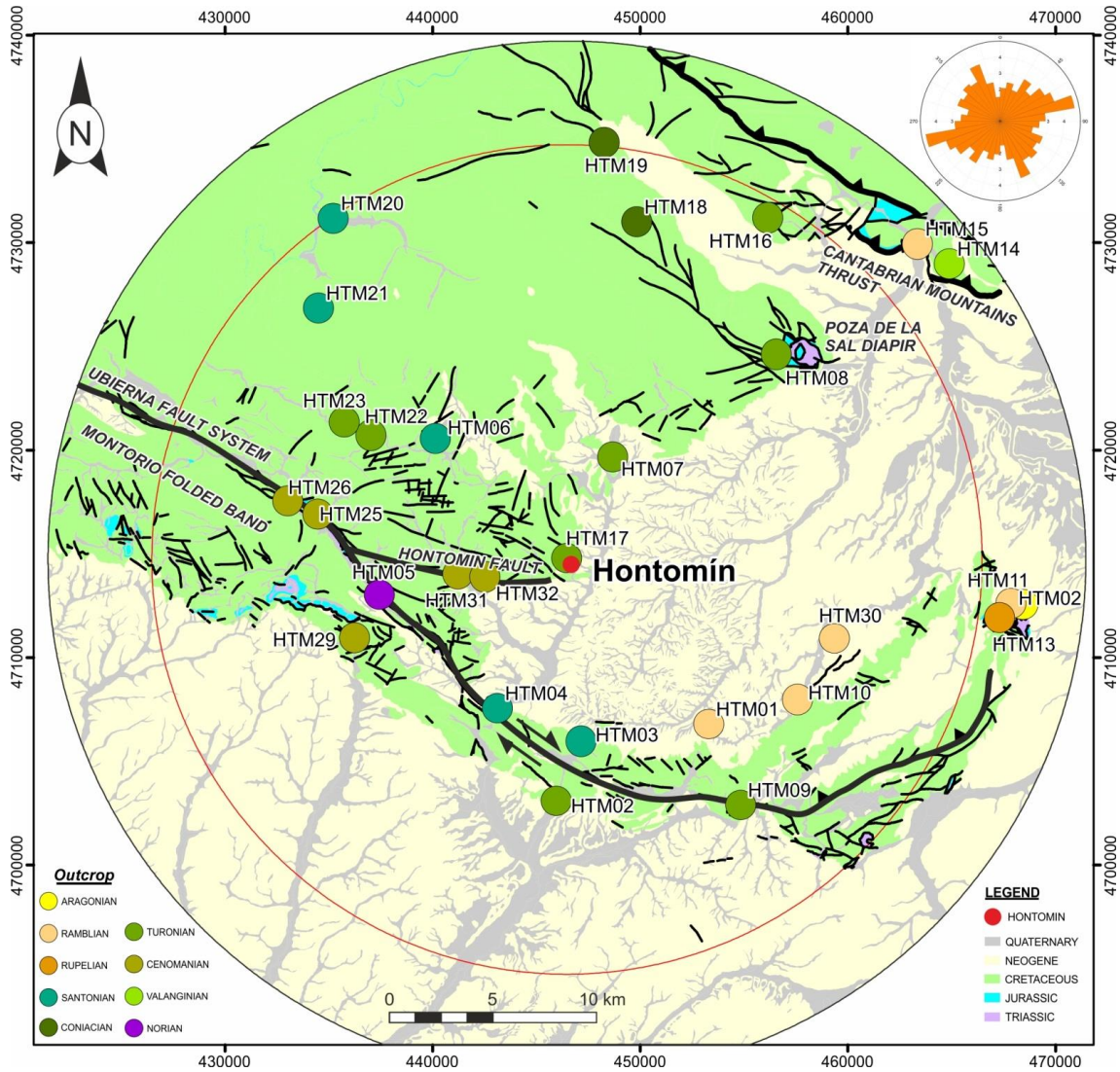


1033

1034

1035 **Figure 4.** Methodology proposed to obtain the strain field affecting the GSC reservoir.
 1036 The distances for outcrops and quadrants proposed is 20 km. The technique of Right
 1037 Dihedral and the K' strain diagram is described in the main text. The e_y and e_x
 1038 represented are a model for explaining the methodology. Dey and Dex are the direction
 1039 of the maximum and minimum strain, respectively. Blue box at the center is the CO_2
 1040 storage geological underground formation.

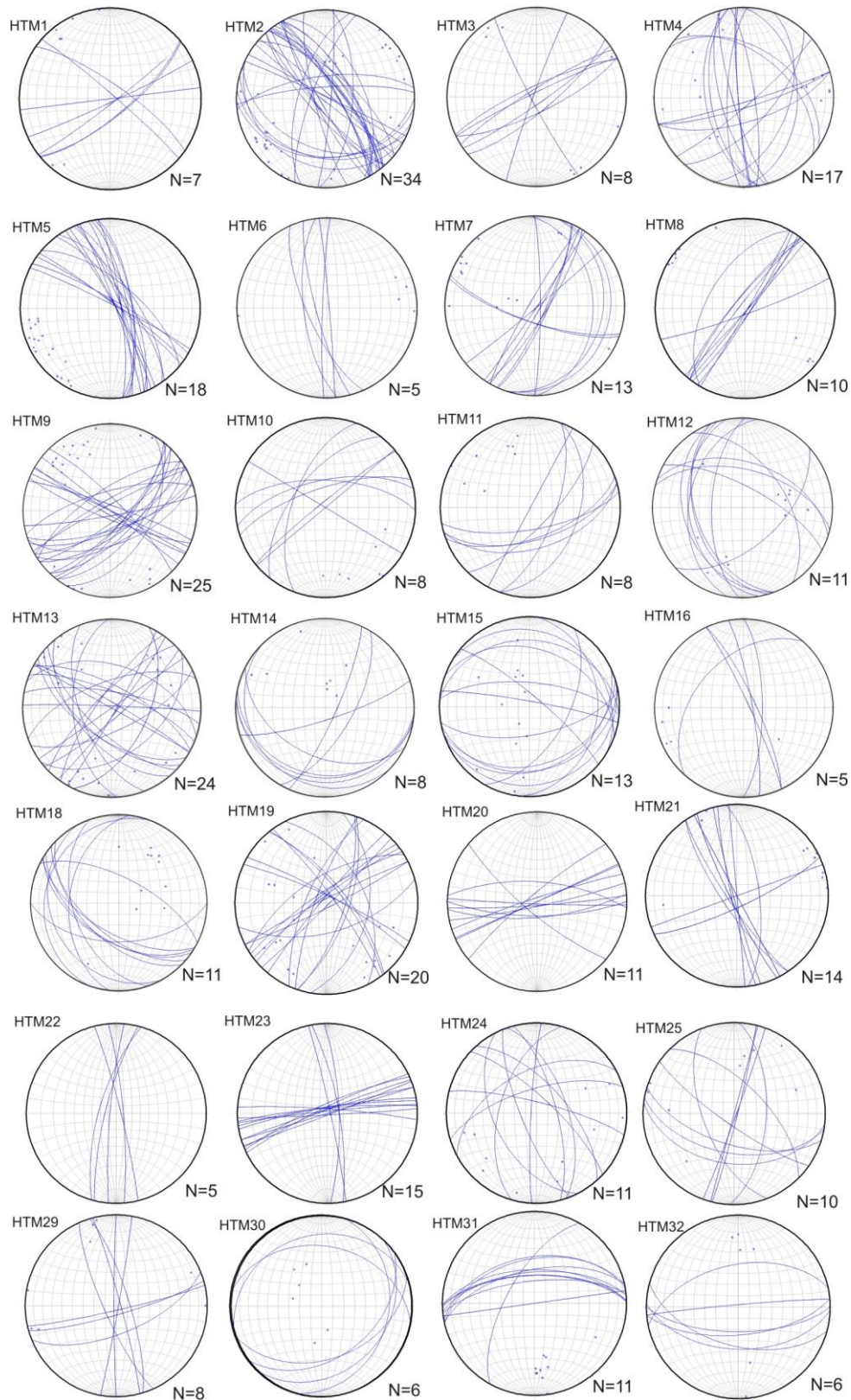
1041



1042

1043

1044 **Figure 5.** Geographical location of field outcrops in the eastern part of the Burgalesa
 1045 Platform domain. Black lines: observed faults; red circle: 20km radius study zone. Rosd
 1046 diagram are the fault orientations from the map. A total of 447 fault data were collected
 1047 in 32 outcrops. Data were measured by a tectonic compass on fault planes at outcrops.
 1048 The spatial distribution of the field stations is constrained by the lithology. Coordinates
 1049 are in meters, UTM H30.



1050

1051 **Figure 6.** Stereographic representation (cyclographic plot in Schmidt net, lower
 1052 hemisphere) of the fault planes measured in the field stations. “n” is the number of
 1053 available data for each geostructural station. HTM24, 27, 28 are not included due to
 1054 lack of data, and HTM17 due to the high number of faults.

1055

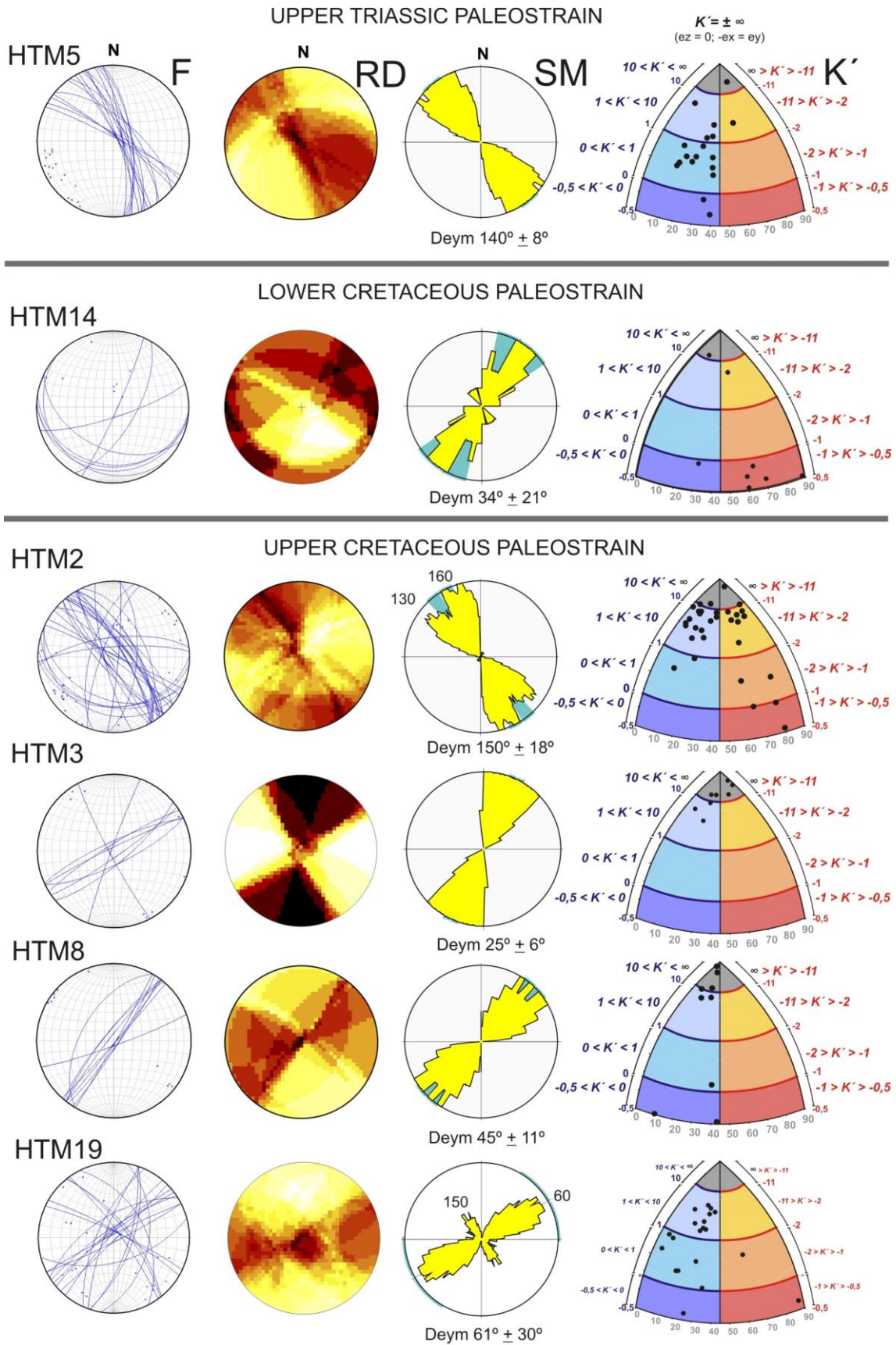
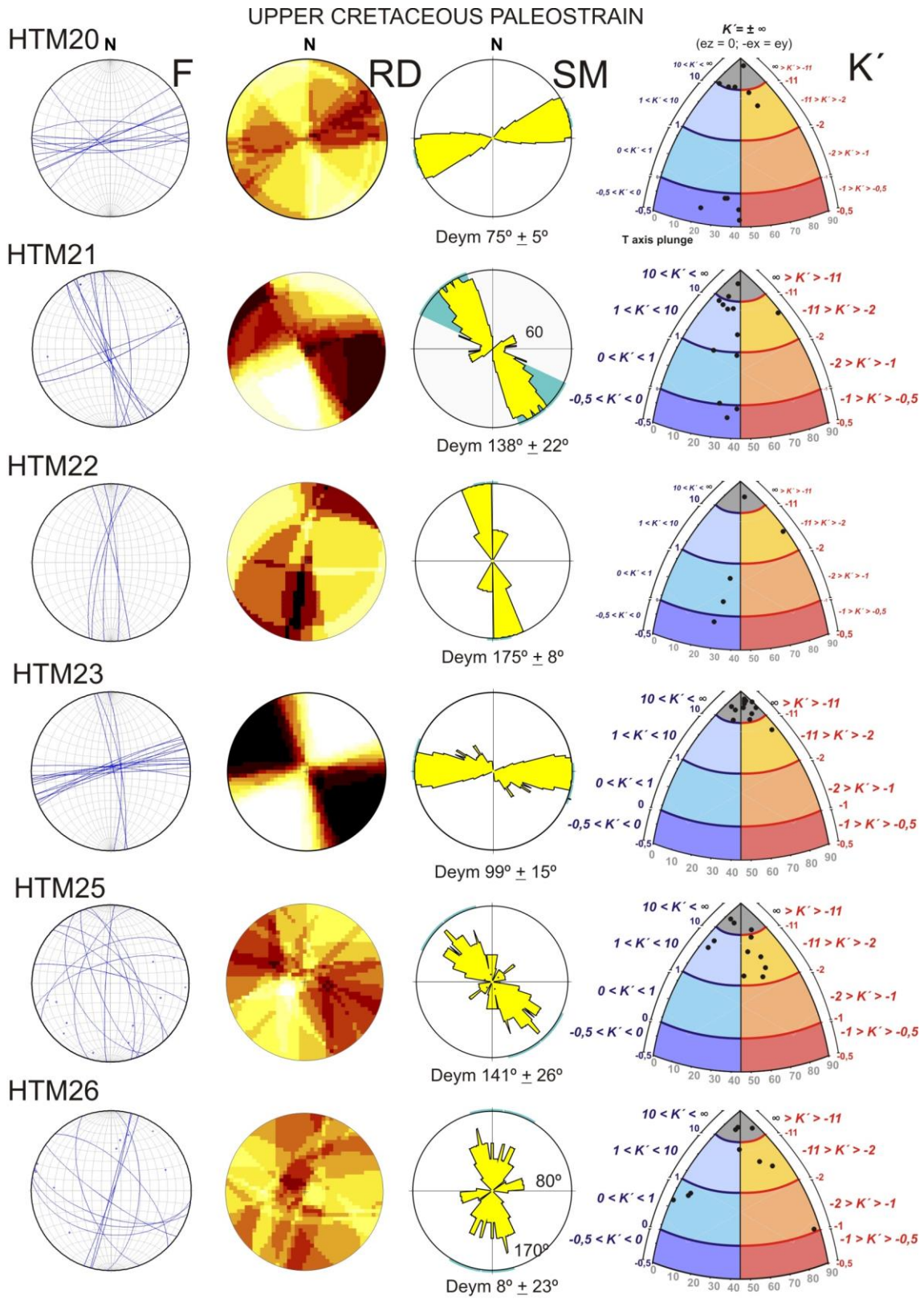


FIGURE 7a

1056

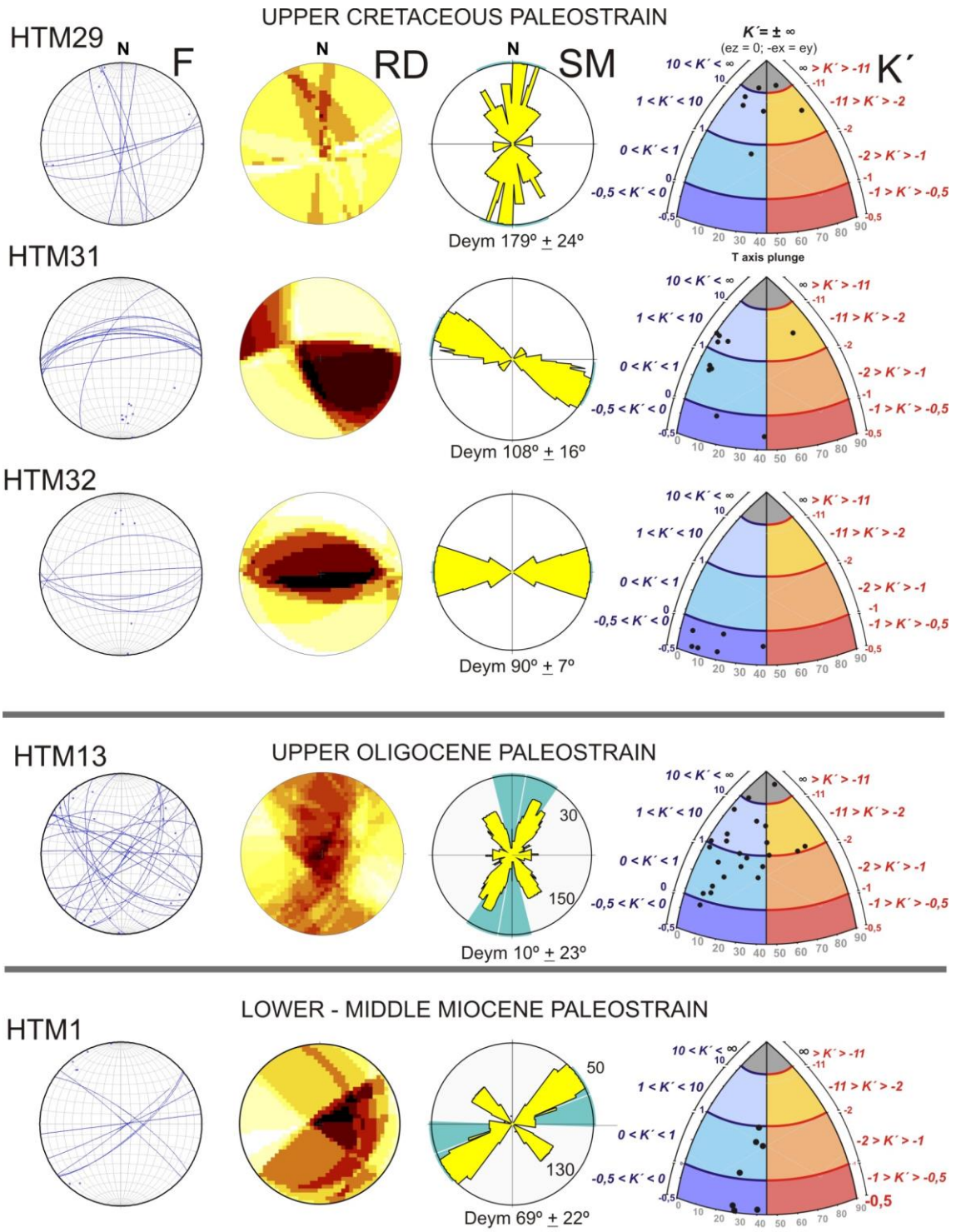
1057



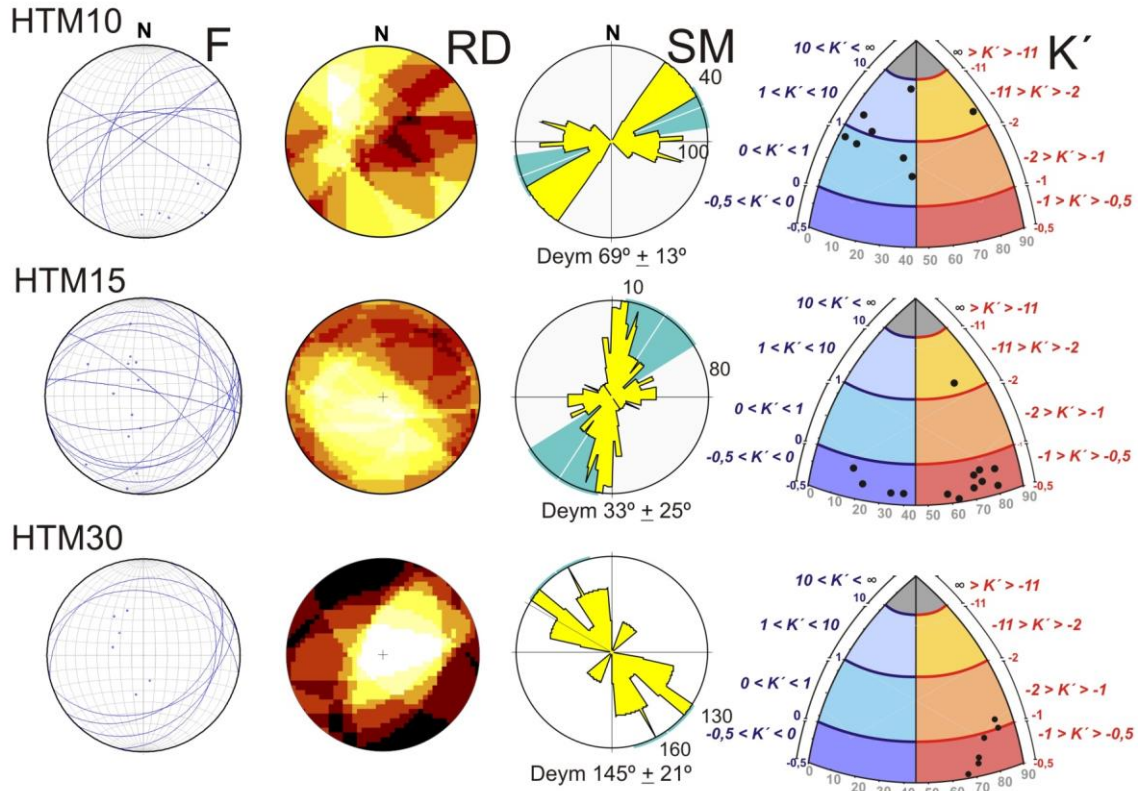
1058

1059

1060



LOWER - MIDDLE MIOCENE PALEOSTRAIN



MIDDLE MIOCENE PALEOSTRAIN

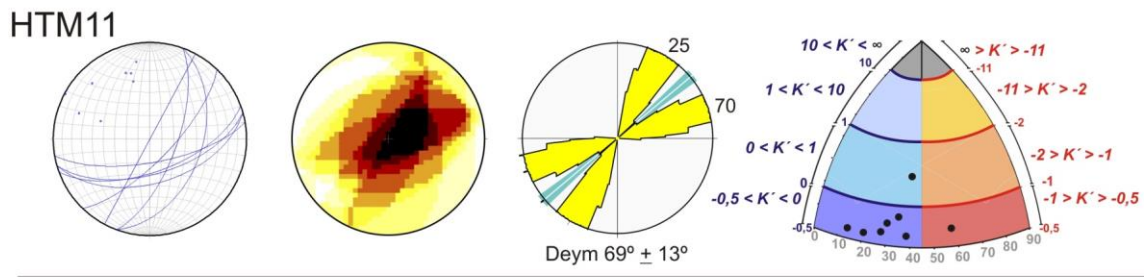
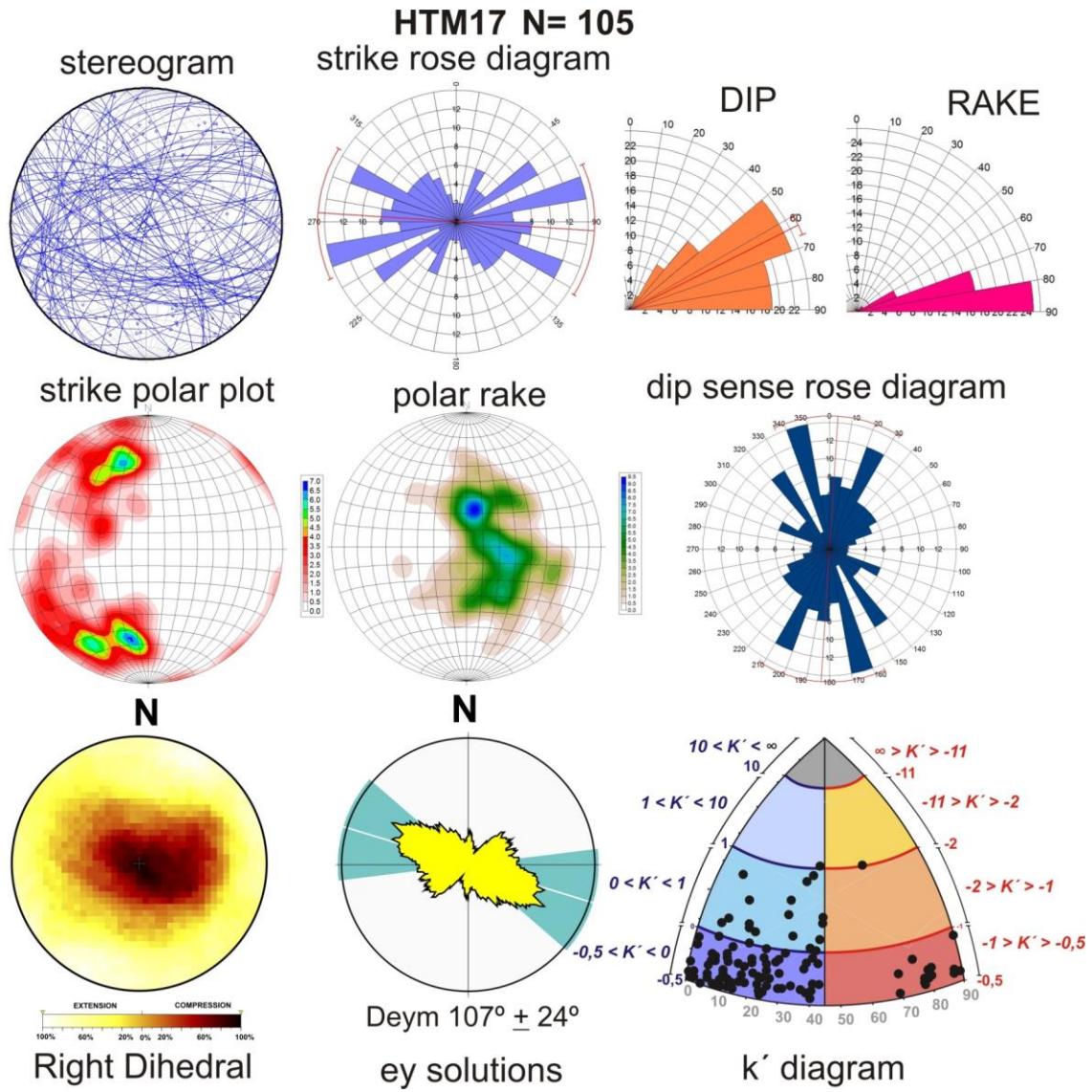


FIGURE 7d

1063

1064

1065 **Figure 7.** Results of the paleostrain analysis obtained and classified by age. Deym:
 1066 striking of the averaged of the Dey value; F: fault stereographic representation; K':
 1067 diagram with dots for each fault slip solution; RD: Right Dihedral method; SM: Slip
 1068 Method, K'. See Methods for further explanation.

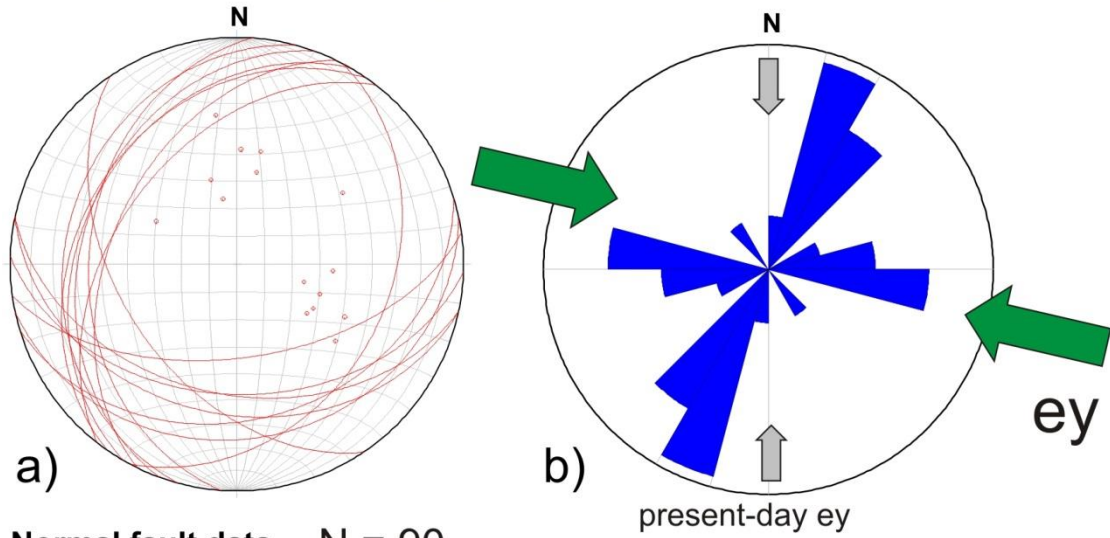


1069
1070
1071
1072
1073

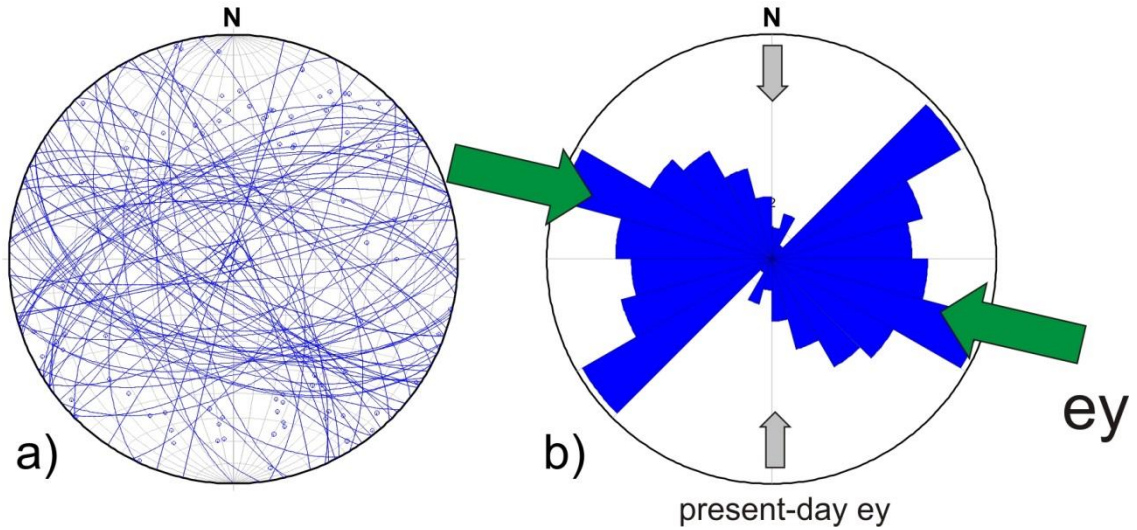
Figure 8. Fault data from the outcrop HTM17 located on top of the HPP. See figure 5 for the geographical location. Stereogram plot is lower hemisphere and Schmidt net.

HTM17

Reverse fault data N = 15



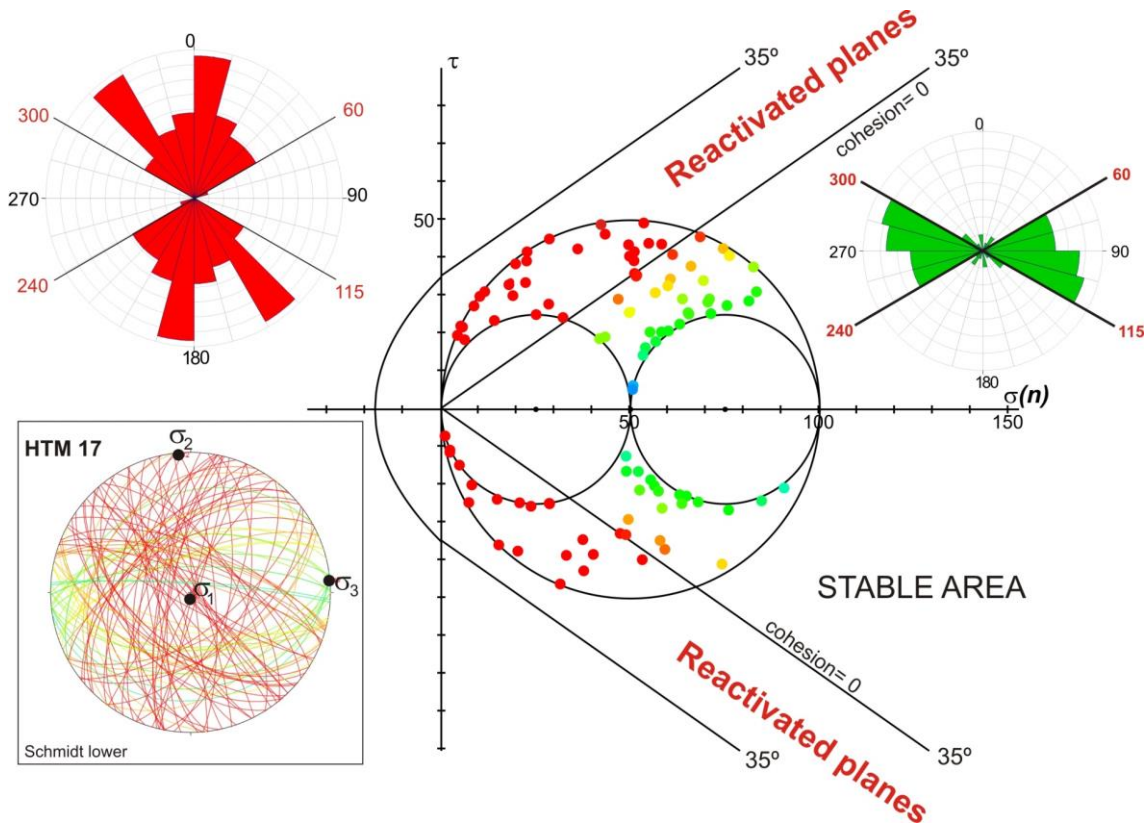
Normal fault data N = 90



1074

1075

1076 **Figure 9.** Normal and reverse faults stereograms (lower hemisphere and Schmidt net),
1077 and rose diagrams measured in HTM17. Green arrows indicate the orientation of the
1078 local paleostrain field. Grey arrows indicate the orientation of the present-day regional
1079 stress field (Herraiz et al., 2000).

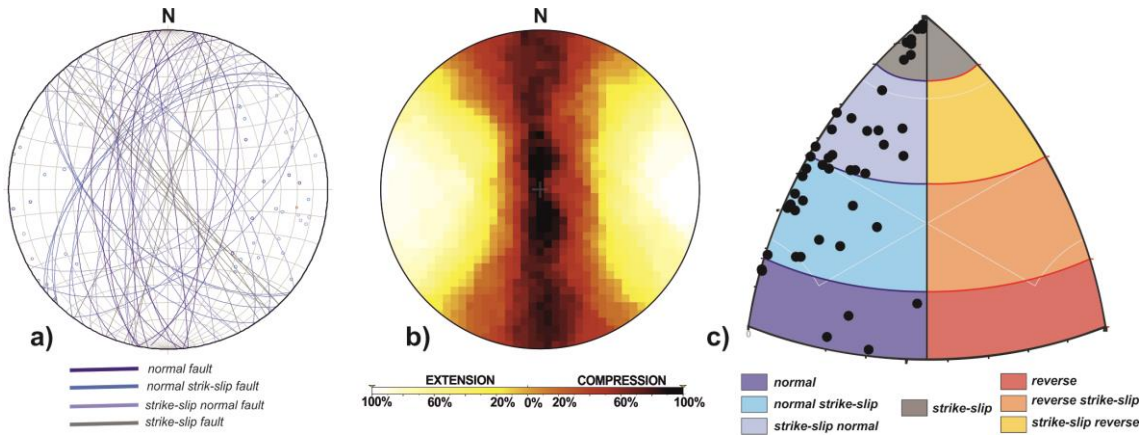


1080

1081

1082 **Figure 10.** Mohr-Coulomb failure analysis for the fault-slip data measured in HTM17
 1083 under the present-day stress tensor determined by Herraiz et al. (2000). Red dots are
 1084 faults reactivated, and green and orange dots are located within the stable zone. Red
 1085 rose diagram shows the orientation of reactivated faults, between N-S to N60°E and
 1086 from N115°E to N180°E. Green rose diagram shows the fault orientation for faults non-
 1087 reactivated under the active tress field within the area. See text for further details. The
 1088 yellow data in the M-C diagrams are referred to those planes close to be reactivated, and
 1089 potentially reactivated by increasing the pore pressure.

1090



1091

1092

1093 **Figure 11.** a) Stereogram and poles of fault sets (HTM17) reactivated under the present-

1094 day stress field suggested by Herraiz et al. (2000). b) Right-Dihedral of the reactivated

1095 fault sets. c) K'-strain diagram showing the type of fault for each fault-set.

1096

1097 **TABLE CAPTIONS**

K'	T -axis	strain axis rel.	fault type	tectonic field
< -0.5	0°	$e_z > e_x = -e_y$	normal	pure radial extension
$-0.5 < K' < 0$	$0^\circ-45^\circ$	$e_z > -e_x > -e_y$	normal	radial extension
$K' = 0$	$0^\circ-45^\circ$	$e_z = -e_x, e_y = 0$	normal	plain strain
$0 < K' < 1$	$0^\circ-45^\circ$	$-e_x > e_z > e_y$	normal with SS	extension with shear
$k=1$	$0^\circ-45^\circ$	$-e_x > e_y = e_z$	normal with SS	extension with shear
$1 < K' < 10$	$0^\circ-45^\circ$	$-e_x > e_y > e_z$	strike-slip with N	shear with extensional
$10 < K' < \infty$	$0^\circ-45^\circ$	-----	strike-slip	shear deformation
$K' = \infty$	45°	$e_z = 0; -e_x = e_y$	strike-slip	pure shear deformation
$\infty < K' < -11$	$45^\circ-90^\circ$	-----	strike-slip	shear deformation
$-11 < K' < -2$	$45^\circ-90^\circ$	$e_y > -e_x > -e_z$	strike-slip with R	shear with compression
$K' = -2$	$45^\circ-90^\circ$	$e_y > -e_x = -e_z$	reverse with SS	compression with shear
$-2 < K' < -1$	$45^\circ-90^\circ$	$e_y > -e_z > -e_x$	reverse with SS	compression with shear
$K' = -1$	$45^\circ-90^\circ$	$-e_z = e_y, e_x = 0$	reverse	plain strain
$-1 < K' < -0.5$	$45^\circ-90^\circ$	$-e_z > e_y > e_x$	reverse	radial compression
$K' = -0.5$	$45^\circ-90^\circ$	$-e_z > e_y = e_x$	reverse	pure radial compression

SS = strike-slip
 N = normal
 R = reverse
 e_x = value of the minimum horizontal shortening
 e_y = value of the maximum horizontal shortening
 e_z = value of the vertical axis

1098

1099 **Table 1.** Different tectonic regimes, K' values, dip values and fault type for the
 1100 Kaverina modified diagram used in this work. According to the strain axes relationship,
 1101 faults can be classified and the tectonic regime can be established.

1102

STATION	n ^o faults	series/epoch	Dey (°)	dispersion	strain tensor
HTM11	8	MIDDLE MIOCENE	50	4	NORMAL STRIKE-SLIP
HTM30	6	EARLY-MIDDLE MIOCENE	145	21	COMPRESSION
HTM15	13	EARLY-MIDDLE MIOCENE	33	25	COMPRESSION
HTM10	8	EARLY-MIDDLE MIOCENE	69	13	NORMAL STRIKE-SLIP
HTM01	7	EARLY-MIDDLE MIOCENE	70	22	NORMAL STRIKE-SLIP
HTM13	24	EARLY OLIGOCENE	25-160	23	NORMAL STRIKE-SLIP
HTM32	6	UPPER CRETACEOUS	90	7	NORMAL
HTM31	11	UPPER CRETACEOUS	108	16	STRIKE-SLIP NORMAL
HTM29	8	UPPER CRETACEOUS	179	24	STRIKE-SLIP NORMAL
HTM26	10	UPPER CRETACEOUS	0	23	STRIKE-SLIP
HTM25	11	UPPER CRETACEOUS	141	26	STRIKE-SLIP COMPRESSION
HTM23	14	UPPER CRETACEOUS	99	15	STRIKE-SLIP
HTM22	5	UPPER CRETACEOUS	175	8	NORMAL STRIKE-SLIP
HTM21	14	UPPER CRETACEOUS	138	22	STRIKE-SLIP NORMAL
HTM20	11	UPPER CRETACEOUS	75	5	STRIKE-SLIP
HTM19	20	UPPER CRETACEOUS	61	30	NORMAL STRIKE-SLIP
HTM17	105	UPPER CRETACEOUS	107	24	NORMAL
HTM08	10	UPPER CRETACEOUS	45	11	STRIKE-SLIP
HTM3	8	UPPER CRETACEOUS	25	6	STRIKE-SLIP (N-C)
HTM2	34	UPPER CRETACEOUS	150	18	STRIKE-SLIP (N-C)
HTM14	8	LOWER CRETACEOUS	34	21	COMPRESSION
HTM5	18	UPPER TRIASSIC	140	8	NORMAL STRIKE-SLIP

1103

1104 **Table 2.** Summary of the outcrops showing the number of faults, the type of the strain
 1105 tensor obtained, the Dey, S_{Hmax} striking and the age of the affected geological materials.
 1106 N-C is normal component for strike-slip movement.

1107